

Proximate Quantum Spin Liquid on Designer Lattice

Xiaoran Liu,* Sobhit Singh, Victor Drouin-Touchette, Tomoya Asaba, Jess Brewer, Qinghua Zhang, Yanwei Cao, Banabir Pal, Srimanta Middey, P. S. Anil Kumar, Mikhail Kareev, Lin Gu, D. D. Sarma, Padraic Shafer, Elke Arenholz, John W. Freeland, Lu Li, David Vanderbilt, and Jak Chakhalian



Cite This: <https://dx.doi.org/10.1021/acs.nanolett.0c04498>



Read Online

ACCESS |

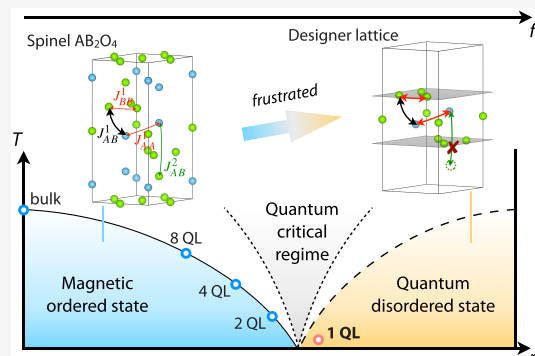
Metrics & More

Article Recommendations

Supporting Information

ABSTRACT: Complementary to bulk synthesis, here we propose a designer lattice with extremely high magnetic frustration and demonstrate the possible realization of a quantum spin liquid state from both experiments and theoretical calculations. In an ultrathin (111) CoCr_2O_4 slice composed of three triangular and one kagome cation planes, the absence of a spin ordering or freezing transition is demonstrated down to 0.03 K, in the presence of strong antiferromagnetic correlations in the energy scale of 30 K between Co and Cr sublattices, leading to the frustration factor of ~ 1000 . Persisting spin fluctuations are observed at low temperatures via low-energy muon spin relaxation. Our calculations further demonstrate the emergence of highly degenerate magnetic ground states at the 0 K limit, due to the competition among multiply altered exchange interactions. These results collectively indicate the realization of a proximate quantum spin liquid state on the synthetic lattice.

KEYWORDS: ultrathin films, frustration, spin liquids, emergent magnetism



In a magnetic crystal, the basic notion of minimizing free energy necessitates that after cooling down to sufficiently low temperature all spins should lock into a long-range ordered pattern. However, on a lattice where the exchange interactions between localized spins cannot be simultaneously satisfied, the system becomes magnetically frustrated with the tendency of forming unusual disordered phases significantly different from a simple paramagnet.^{1–5} Furthermore, in recent years from a theory standpoint the combination of electronic correlations, quantum fluctuations, spin–orbit couplings, and lattices supporting frustrated magnetic interactions has been a remarkably fertile ground for predicting unconventional entangled states of quantum matter including magnetic monopoles in spin ice, topological superconductor, axion insulator, Weyl semimetal, magnetic fragmentation, and a variety of liquid-like spin states.^{6–23} A quantum spin liquid (QSL) belongs to one of these exotic states; generally, it possesses no long-range magnetic order, lacks any spontaneously broken symmetry, and carries a spectrum of fractional excitations.^{24–27}

As for the experimental realization of a QSL, the currently existing “recipes” are illuminating but limited.^{28–34} On one hand, a general guiding principle is that in order to reach a QSL, significant frustration resulting either from the lattice geometry, multiple exchange terms, or bond conflict is an essential prerequisite.³¹ After tremendous decades-long efforts, promising candidate materials have been proposed and synthesized, including the prototypical examples of the widely

studied organic salts $\text{EtMe}_3\text{Sb}[\text{Pd}(\text{dmit})_2]_2$ and $\kappa-(\text{ET})_2\text{Cu}_2(\text{CN})_3$,¹⁹ the herbertsmithite $\text{ZnCu}_3(\text{OH})_6\text{Cl}_2$ and barlowite $\text{Cu}_3\text{Zn}(\text{OH})_6\text{FBr}$,²⁹ and the Kitaev QSLs $\alpha\text{-RuCl}_3$ and A_2IrO_3 ($\text{A} = \text{Na}, \text{Li}$).³² On the other hand, however, the underlying lattices of almost all known QSLs are bound to five types of geometries, namely, triangular, pyrochlore, kagome, hyperkagome, and honeycomb lattices.^{24,30,33} This in turn limits the pursuit of novel QSL candidates and brings to the focus open questions of whether any additional lattice motifs can host a QSL and how can it be achieved experimentally.

In recent years, complementary to bulk synthesis, heteroepitaxial engineering of ultrathin films, multilayers, and superlattices by means of advanced deposition techniques have been developed into a powerful platform for materials design and innovation.^{35–41} In particular, geometrical lattice engineering principally aiming at the design and fabrication of lattices with artificial geometry by stacking on demand a specific number of atomic planes along unconventional crystallographic directions has been recognized as a promising path to emergent phenomena.^{42–48} This framework once

Received: November 16, 2020

Revised: February 16, 2021

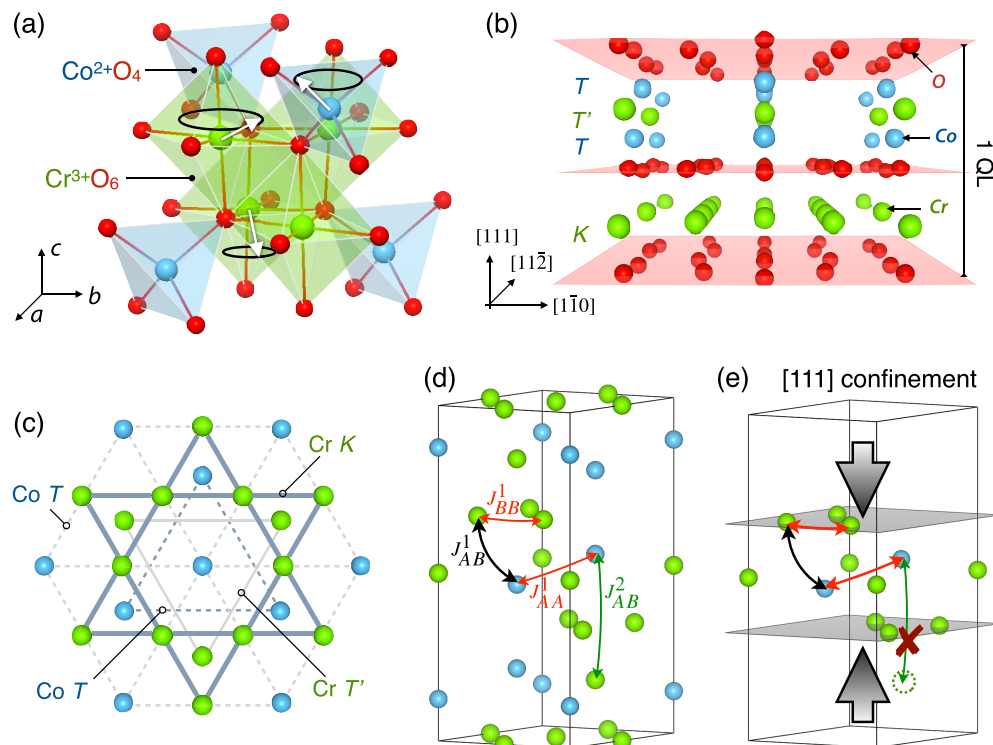


Figure 1. (a) Schematic representation of bulk CoCr₂O₄ composed of networks of Co²⁺O₄ tetrahedra and Cr³⁺O₆ octahedra. The arrows depict the conical spin configuration of the ground state. (b) Definition of one quadruplet layer (1 QL) of CoCr₂O₄ along the [111] direction, including four alternative cation planes: kagome Cr plane (K), triangle Co plane (T), triangle Cr plane (T'), and triangle Co plane (T). Note that such a quasi-2D lattice motif does not naturally exist, nor it can be realized via exfoliation of bulk crystals. (c) [111] top view of the alternative cation planes in 1 QL. (d) Magnetic exchange pathways in (111)-oriented CoCr₂O₄. (e) Effects of confinement on the exchange couplings in 1 QL CoCr₂O₄.

experimentally validated can offer an alternative approach for creating new classes of synthetic lattices, potentially hosting QSL and other intriguing states of quantum matter.

In this Letter, we address these challenges and propose a generic design of a novel quasi-two-dimensional (quasi-2D) lattice derived from the spinel structure and demonstrate its feasibility for supporting a QSL phase from both comprehensive sets of experiments and theoretical calculations. We note that although our system is an $S > 1/2$ system, its spin-fluctuation dynamics is still far from the large S limit, and the spins, in principle, can exhibit quantum features.^{49–51} Concretely, using CoCr₂O₄ as a prototype, we fabricated a series of (111)-oriented ultrathin films, confined by non-magnetic Al₂O₃ layers into a quantum well geometry. Compared to its bulk counterpart, the onset of the ferrimagnetic transition decreases monotonically with reduced thickness and eventually shuts off in a single-unit slab of (111) CoCr₂O₄. In this quasi-2D limit, the degree of magnetic frustration becomes enhanced by almost 3 orders of magnitude with persisting spin fluctuations down to 30 mK. Our first-principles density functional theory (DFT) calculations and classical Monte Carlo (MC) simulations on this designer lattice reveal the presence of strongly frustrated magnetic configurations with a tremendous degree of degeneracy, which prevents the system from achieving a definite long-range ordering at 0 K limit. These combined results imply the realization of a proximate QSL in the single-unit (111) CoCr₂O₄ slice.

CoCr₂O₄ belongs to the normal spinel (AB_2O_4) chromite family, MCr₂O₄ (M = Mn, Fe, Co, and Ni)⁵² where the magnetically active M²⁺ ions occupy the tetrahedral A sites of

diamond sublattice and the Cr³⁺ ions occupy the octahedral B sites of pyrochlore sublattice, possessing complex spin configuration of the ground state.⁵³ Specifically, in bulk CoCr₂O₄ [Figure 1a], a collinear ferrimagnetic state first forms with the Curie temperature of ~93 K, which transforms into an incommensurate spiral ferrimagnetic state at ~26 K. An incommensurate to commensurate lock-in transition further takes place at ~14 K.^{54,55} When viewed along the [111] direction, the structure is an intrinsic stacking of triangle (T) and kagome (K) cation planes from Co and Cr ions embedded in the oxygen cubic close-packed frame. This leads to a sequence of “–O–Cr(K)–O–Co(T)–Cr(T')–Co(T)–” in a single unit with four cation layers, which we denote as one quadruplet layer (1 QL) [Figure 1b,c].

Bulk CoCr₂O₄ is weakly frustrated due to the interplay of multiple exchange couplings [Figure 1d]. The most dominant first-neighbor J_{AB}¹ interatomic coupling is antiferromagnetic (AFM), which alone would favor a Néel-type collinear ferrimagnetic ordering. The weak magnetic frustration originates from the competition between J_{AB}¹ and the intraatomic AFM couplings J_{BB}¹ and J_{AA}¹ and is partially relieved by the second-neighbor ferromagnetic coupling J_{AB}². Because of the entwined nature of those couplings, one can conjure that if the lattice is made [111] confined [Figure 1e], the magnetic frustration could be markedly elevated as a result of enhanced geometric frustration from J_{BB}¹ and J_{AA}¹ on kagome and triangle planes plus termination of the out-of-plane J_{AB}², which may collectively trigger the formation of QSL.

On the basis of this design idea, [n QL CoCr₂O₄/1.3 nm Al₂O₃]₄ ($n = 1, 2, 4$; 1 QL \approx 4.8 Å) superlattices were fabricated by pulsed laser deposition on (0001)-oriented single

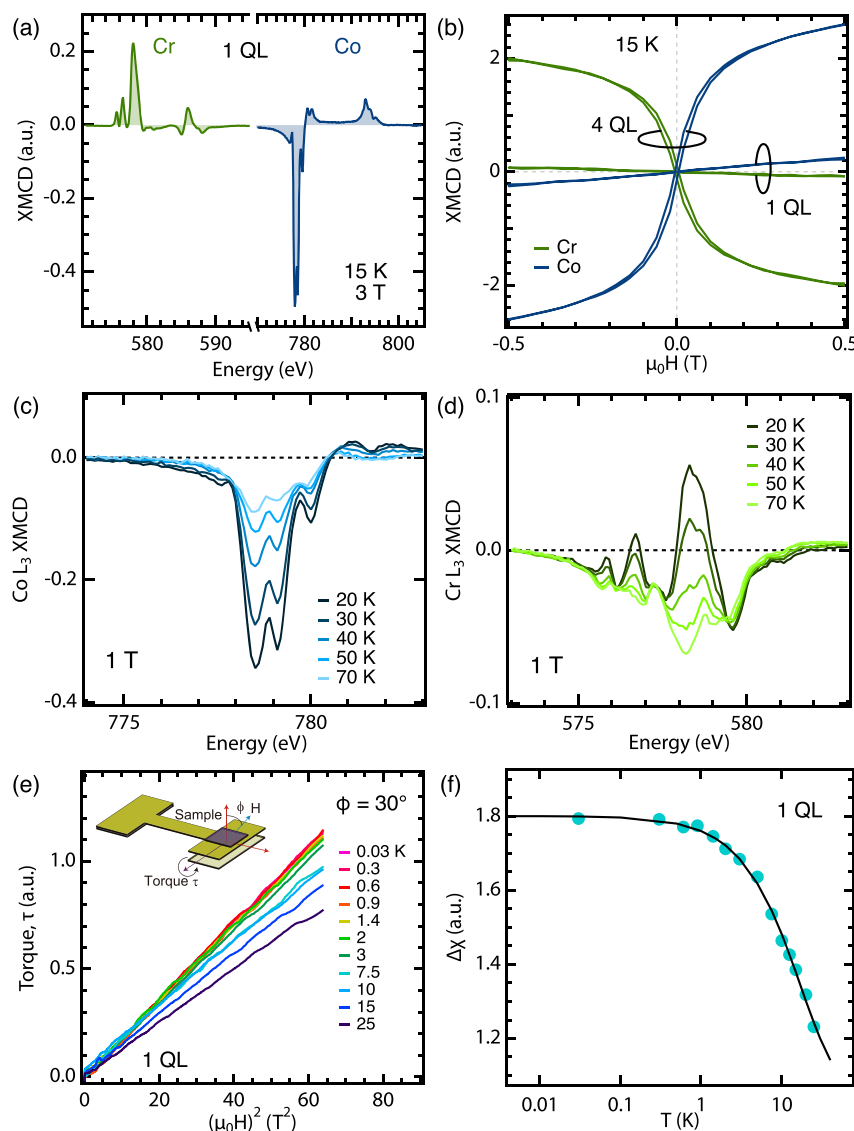


Figure 2. (a) XMCD spectra at L_{2,3} edges of both Co and Cr in 1 QL CoCr₂O₄. (b) Field dependence of the XMCD L₃ intensity of Co (~778 eV) and Cr (~577 eV). Results of both 4 and 1 QL CoCr₂O₄ are shown for comparison. (c,d) Co and Cr L₃ XMCD spectra at various temperatures. (e) Torque magnetometry curves of 1 QL CoCr₂O₄ at the temperatures between 25–0.03 K. (f) Temperature dependence of $\Delta\chi$ extracted from linear fit of the τ versus H^2 curves [$\tau = \Delta\chi(\mu_0 H)^2$] from (e). The solid line is a guide for the eye.

crystal Al₂O₃ substrates. Details of the synthesis and characterization were reported elsewhere.^{56,57} It is noteworthy that, recently, an emergent Yafet-Kittel type ferrimagnetic state due to the enhanced frustration in 4 and 2 QLs of CoCr₂O₄ was reported in ref 48. In this Letter, we primarily focus on the 1 QL case.

First, we start with the investigation of the magnetic behavior of each sublattice by recording the resonant X-ray absorption spectroscopy (XAS) taken with left- and right-circularly polarized beams. The difference between those two spectra, called X-ray magnetic circular dichroism (XMCD), reflects the net magnetization of a specifically probed element.⁵⁸ As shown in Figure 2a, XMCD of both Cr and Co are clearly observed at 15 K with opposite sign, as indicated by the distinct features at the L₃ edges (Cr ~ 577 eV and Co ~ 778 eV). These results confirm that at low temperatures due to the AFM J_{AB}^1 term, the overall orientation of spins on the Co sublattice is along the field, whereas that on the Cr sublattice is against the field. Then at high temperatures where the thermal

energy overcomes the exchange interaction, a paramagnetic state is expected with the orientation of all spins aligned parallel to the external field. This is in fact demonstrated by temperature-dependent XMCD spectra at L₃ edges, where the sign of Cr flips at temperatures above ~30 K [see Figure 2c,d].

With the knowledge about the scale of J_{AB}^1 , we can explore whether a long-range magnetic ordering is present in 1 QL CoCr₂O₄. The J_{AB}^1 term favors a ferrimagnetic state with a ferromagnetic spin arrangement on each sublattice.⁵⁹ As a result, hysteretic behavior is anticipated from field-dependent XMCD scans. As seen in Figure 2b, this is indeed observed in the thicker 4 QL CoCr₂O₄ that exhibits clear hysteresis loops at both Co and Cr L₃ edges, consistent with the previous study that the ground state of 4 QL CoCr₂O₄ hosts an emergent Yafet-Kittel type ferrimagnetic ordering.⁴⁸ However, in sharp contrast no hysteresis loop but a linear XMCD versus H relationship is found on both Co and Cr in 1 QL CoCr₂O₄, typical of a paramagnetic behavior.

In order to further examine if any long-range spin ordering emerges at extremely low temperatures, we performed the torque magnetometry measurements on 1 QL CoCr_2O_4 from 30 K down to 0.03 K. This technique quantifies the magnetic torque response of a sample with respect to the applied magnetic field ($\tau \propto M \times H$) and is an exquisitely sensitive utility to probe vanishingly small magnetic signals from ultrathin samples and interfaces.^{60,61} The result shown in Figure 2e confirms that within the resolution of measurement and entire temperature range, no hysteresis but a reversible parabolic $\tau \propto (\mu_0 H)^2$ relationship is observed for 1 QL, which implies a quantum paramagnetic behavior persisting down to 0.03 K. To make a thorough comparison and eliminate questions about sensitivity of the measurement, we also collected the torque signal on 4 QL CoCr_2O_4 using the same geometry. The data clearly exhibit distinct hysteretic loops (a hallmark of ferro-/ferri-magnetism) appearing below the Curie temperature of 58 K [see SI, Figure S3]. These observations agree well with the field-dependent XMCD results, providing strong evidence for the absence of long-range magnetic ordering in 1 QL CoCr_2O_4 down to 0.03 K. In addition, formation of a spin glass is likely ruled out, as its torque signal usually exhibits a nonparabolic relationship to H .⁶² A combination of these data results in the extremely large frustration factor $f = \Theta_{\text{CW}}/T_C \sim 1000$ in 1 QL, which is almost 3 orders of magnitude larger than that of bulk CoCr_2O_4 ($f \sim 6$).⁶³ Furthermore, it is notable that the extracted anisotropic susceptibility $\Delta\chi$ gradually increases as the temperature decreases and becomes finite and temperature-independent below ~ 1 K, as guided by the solid line in Figure 2f. These results lend strong support for the existence of low-lying magnetic excitations, implying the appearance of nearly degenerate ground states in 1 QL.⁶⁴

Next, we turn to investigate the spin dynamics of 1 QL CoCr_2O_4 by low-energy muon spin relaxation (μSR) spectroscopy from 70 to 4 K in both zero-field (ZF) and 30 G transverse-field (TF) setup. Thanks to its high sensitivity to local fields and capability to characterize the time scale of spin fluctuations, μSR can reliably distinguish between the presence of static moments due to conventional spin ordering or freezing, and dynamical spin moments due to frustration and degeneracy.^{65–72} In ZF- μSR , a simple exponential decay with no oscillatory signal is observed, whereas a slowly relaxing signal precessing at the muon Larmor frequency is clearly observed in all of the TF- μSR spectra (see SI Figure S5 for detailed data). As a result, no coherent precession of the incident μ^+ is found, ruling out the formation of a static uniform local field, characteristic of magnetic phases without long-range ordering (i.e., ferro-/ferri-magnet and commensurate antiferromagnet).⁶⁶

The spin asymmetry and the relaxation rate λ are extracted by fitting the spectra of the time evolution of polarization [see SI for more details], and their temperature dependencies are shown in Figure 3. While below 30 K, the asymmetry decreases with the lowered temperatures, both relaxation rates (in ZF and TF) first increase, reaching a broad “hump” at around 10 K, followed by a reduction again at the base temperatures. These results deem a spin glass transition to be absent because (1) the simple exponential relaxation observed at all temperatures is not the expected form for any type of spin glass;^{73,74} (2) in addition, the ZF- μSR time spectra lack the characteristic “tail” of polarization recovery to one-third, which is expected in spin glasses with static random local fields;⁶⁶ (3) the ZF λ only

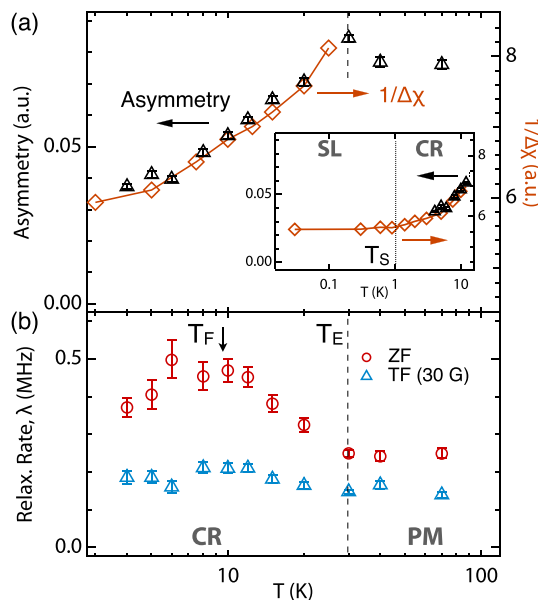


Figure 3. (a) Temperature dependence of the spin asymmetry (left axis) from μ^+ decay and $1/\Delta\chi$ (right axis) from torque measurements on 1 QL CoCr_2O_4 . Inset shows the data at 0.03–10 K with T_S indicating the temperature-independent behavior of $1/\Delta\chi$ below ~ 1 K. (b) Temperature dependence of the μ^+ spin relaxation rate λ from both zero field (red) and 30 G transverse field (blue) measurements. Both asymmetry and λ show a temperature-independent behavior above $T_E \sim 30$ K; below 30 K, λ gradually increases to a broad peak at $T_F \sim 10$ K. PM, CR, and SL represent “paramagnet”, “crossover region”, and “spin liquid”, respectively.

slightly increases from ~ 0.25 MHz at 70 K to 0.35 MHz at 4 K, while below the freezing point of a spin glass, λ typically increases by an order of magnitude ($\lambda \sim 1$ –20 MHz).⁶⁹

From the spin dynamics viewpoint, three characteristic temperatures, T_E , T_F , and T_S appear in 1 QL CoCr_2O_4 [Figure 3]. Specifically, above $T_E \sim 30$ K, the muon spins are mainly depolarized by the rapid fluctuations of local fields due to thermal excitations, leading to both asymmetry and λ as nearly constant, which are conventional paramagnetic features. This observation is also consistent with the XMCD results, indicating the thermal energy overcomes the most dominant J_{AB}^1 at 30 K. Next, asymmetry starts to decrease accompanied by the increase in λ suggesting the slowing down of spin fluctuations due to the onset of J_{AB}^1 , triggering short-range spin–spin correlations between Co and Cr ions. We recap that the local moments of both Co^{2+} ($S = 3/2$) and Cr^{3+} ($S = 3/2$) are $\sim 3.7 \mu_B$, which should correspond to a local distribution ~ 4500 G for a fully static spin.⁷⁵ In contrast, we observed a field of only ~ 500 G, which corresponds to a static moment $\sim 0.4 \mu_B$ only. This indicates that majority of the Co and Cr moments do not freeze and remain fluctuating at finite frequency down to 4 K.

At this point, it is interesting to compare $\Delta\chi$ deduced from the torque data with the local spin susceptibility sensed by muons. As shown in Figure 3a, the trend in spin asymmetry very closely resembles that of the inverse $\Delta\chi$. Namely, it monotonically drops to about 50% at 4 K and becomes practically temperature-independent below $T_S \sim 1$ K. Thus, we can conjecture that below 1 K the spins are entangled all over the sample with persisting dynamics of spin fluctuations. On the other hand, the relaxation rates also have a tendency to level off at very low temperatures. This behavior in λ is similar

to that of several well-characterized gapless QSL candidates including both $S = 1/2$ and $S > 1/2$ systems.^{76–81}

To obtain a microscopic insight into how the designer lattice topology and quantum confinement alter the exchange interactions and consequently the magnetic ground state, we performed DFT calculations and MC simulations on bulk, 2 and 1 QL CoCr₂O₄. We calculate the normalized strength of each exchange term J_{ij}^N/J_{AB}^1 . As shown in Figure 4, toward the

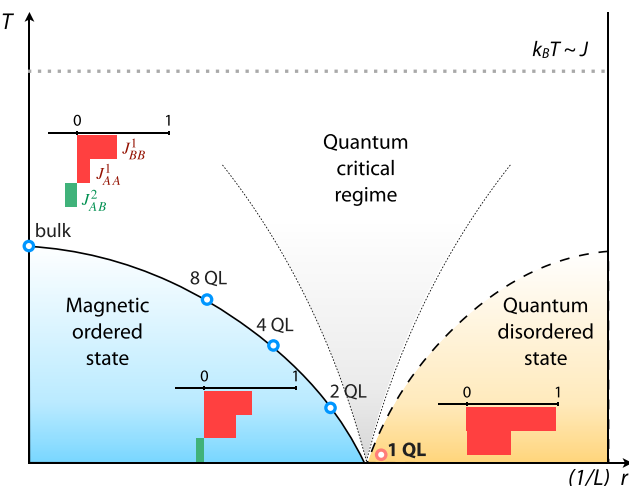


Figure 4. Evolution of the magnetic states of n QL CoCr₂O₄ mapped onto a generic diagram of quantum phase transition. r refers to a nonthermal control parameter (in this case, $1/L$, inverse of the out-of-plane dimension). For bulk, $n = 2$ and $n = 1$, the normalized strength of each exchange coupling (J_{ij}^N/J_{AB}^1) is exhibited by the bar chart; red (green) color indicates AFM (FM) coupling.

2D limit ($1/L \rightarrow \infty$), it is striking that the relative strengths of J_{BB}^1 and J_{AA}^1 , which act to enhance frustration, increase, whereas the contribution of J_{AB}^2 , which tends to relieve frustration, rapidly decreases. The computational data reveal this key effect is a consequence of the markedly smaller number of second-neighbor interactions along (111) in the ultrathin films compared to bulk. In fact, for 1 QL CoCr₂O₄ with J_{AB}^2 completely suppressed, J_{BB}^1 and J_{AA}^1 reach almost the same scale as J_{AB}^1 , in contrast to the behavior in the bulk. This trend agrees very well with the experiments which evidently indicates the presence of extremely large magnetic frustration in 1 QL. Additionally, our classical MC simulations lend further support to this claim, affirming the presence of a paramagnetic phase with a plethora of competing magnetic ground states in 1 QL CoCr₂O₄ [see SI Figures S9–S11].

Finally, we can map the ground state of the n QL CoCr₂O₄ system onto a generic quantum phase transition diagram.^{19,82} In the bulk ($n \rightarrow \infty$), the ground state is a well-defined long-range magnetically ordered state. As n is reduced, it becomes more and more difficult to stabilize a conventional ordered state due to the enhancement of magnetic frustration. Eventually the ground state becomes highly degenerate in 1 QL CoCr₂O₄, unleashing dynamical spin fluctuations. We note this is the regime where quantum effects play a pivotal role in bringing the system into a proximate QSL state without a spin gap.

To summarize, we proposed a general design protocol for novel nonbipartite lattices supporting QSL and demonstrated its realization in 1 QL CoCr₂O₄ where the magnetic frustration is profound and the ground state is highly degenerate with

robust spin fluctuations. Our findings call for further investigation on the excitation spectrum and open a window to a versatile class of new synthetic QSL candidates.

ASSOCIATED CONTENT

Supporting Information

The Supporting Information is available free of charge at <https://pubs.acs.org/doi/10.1021/acs.nanolett.0c04498>.

Additional information regarding sample fabrication, synchrotron XAS and XMCD, torque magnetometry measurements, μ SR experiments, DFT calculations, and Monte Carlo Simulations (PDF)

AUTHOR INFORMATION

Corresponding Author

Xiaoran Liu – Department of Physics and Astronomy, Rutgers University, Piscataway, New Jersey 08854, United States; orcid.org/0000-0003-0938-6109; Email: xiaoran.liu@rutgers.edu

Authors

Sobhit Singh – Department of Physics and Astronomy, Rutgers University, Piscataway, New Jersey 08854, United States

Victor Drouin-Touchette – Department of Physics and Astronomy, Rutgers University, Piscataway, New Jersey 08854, United States

Tomoya Asaba – Department of Physics, University of Michigan, Ann Arbor, Michigan 48109, United States

Jess Brewer – TRIUMF, Vancouver, British Columbia, Canada V6T 2A3; Department of Physics and Astronomy, University of British Columbia, Vancouver, British Columbia, Canada V6T 1Z1

Qinghua Zhang – Beijing National Laboratory for Condensed-Matter Physics and Institute of Physics, Chinese Academy of Sciences, Beijing 100190, P.R. China

Yanwei Cao – Ningbo Institute of Materials Technology and Engineering, Chinese Academy of Sciences, Ningbo, Zhejiang 315201, China

Banabir Pal – Department of Physics and Astronomy, Rutgers University, Piscataway, New Jersey 08854, United States; Solid State and Structural Chemistry Unit, Indian Institute of Science, Bengaluru 560012, India

Srimanta Middey – Department of Physics, Indian Institute of Science, Bengaluru 560012, India; orcid.org/0000-0001-5893-0946

P. S. Anil Kumar – Department of Physics, Indian Institute of Science, Bengaluru 560012, India; orcid.org/0000-0002-4574-0868

Mikhail Kareev – Department of Physics and Astronomy, Rutgers University, Piscataway, New Jersey 08854, United States

Lin Gu – Beijing National Laboratory for Condensed-Matter Physics and Institute of Physics, Chinese Academy of Sciences, Beijing 100190, P.R. China; orcid.org/0000-0002-7504-031X

D. D. Sarma – Solid State and Structural Chemistry Unit, Indian Institute of Science, Bengaluru 560012, India

Padraic Shafer – Advanced Light Source, Lawrence Berkeley National Laboratory, Berkeley, California 94720, United States; orcid.org/0000-0001-9363-2557

Elke Arenholz – Advanced Light Source, Lawrence Berkley National Laboratory, Berkeley, California 94720, United States

John W. Freeland – Advanced Photon Source, Argonne National Laboratory, Argonne, Illinois 60439, United States

Lu Li – Department of Physics, University of Michigan, Ann Arbor, Michigan 48109, United States

David Vanderbilt – Department of Physics and Astronomy, Rutgers University, Piscataway, New Jersey 08854, United States

Jak Chakhalian – Department of Physics and Astronomy, Rutgers University, Piscataway, New Jersey 08854, United States

Complete contact information is available at:
<https://pubs.acs.org/10.1021/acs.nanolett.0c04498>

Notes

The authors declare no competing financial interest.

ACKNOWLEDGMENTS

The authors deeply acknowledge D. Khomskii, G. Fiete, X. Hu, P. Coleman, K. Rabe, P. Chandra, and P. Mahadevan for numerous insightful discussions and A. Suter and P. Thomas for their assistance on the μ SR experiments. X.L. and J.C. acknowledge the support by the Gordon and Betty Moore Foundation EPiQS Initiative through Grant GBMF4534, and by the Department of Energy under Grant DE-SC0012375. S.S. and D.V. acknowledge the support from ONR Grant N00014-16-1-2951. V.D.-T. is supported by DOE grant DE-FG02-99ER45790 and is thankful for the support of the Fonds de Recherche Quebecois en Nature et Technologie. This work of L.L. at Michigan is mainly supported by the Department of Energy under Award No. DE-SC0020184 (torque magnetometry measurements). This research used resources of the Advanced Light Source, which is a Department of Energy Office of Science User Facility under Contract No. DE-AC0205CH11231. This research used resources of the Advanced Photon Source, a U.S. Department of Energy Office of Science User Facility operated by Argonne National Laboratory under Contract No. DE-AC02-06CH11357.

REFERENCES

- (1) Ramirez, A. P. Strongly geometrically frustrated magnets. *Annu. Rev. Mater. Sci.* **1994**, *24*, 453–480.
- (2) Greedan, J. Geometrically frustrated magnetic materials. *J. Mater. Chem.* **2001**, *11*, 37–53.
- (3) Bramwell, S. T.; Gingras, M. J. P. Spin ice state in frustrated magnetic pyrochlore materials. *Science* **2001**, *294*, 1495–1501.
- (4) Nisoli, C.; Moessner, R.; Schiffer, P. Colloquium: artificial spin ice: designing and imaging magnetic frustration. *Rev. Mod. Phys.* **2013**, *85*, 1473.
- (5) Starykh, O. A. Unusual ordered phase of highly frustrated magnets: a review. *Rep. Prog. Phys.* **2015**, *78*, 052502.
- (6) Lee, P. From high temperature superconductivity to quantum spin liquid: progress in strong correlation physics. *Rep. Prog. Phys.* **2008**, *71*, 012501.
- (7) Meng, Z. Y.; Lang, T. C.; Wessel, S.; Assaad, F. F.; Muramatsu, A. Quantum spin liquid emerging in two-dimensional correlated Dirac fermions. *Nature* **2010**, *464*, 847–851.
- (8) Pratt, F. L.; Baker, P. J.; Blundell, S. J.; Lancaster, T.; Ohira-Kawamura, S.; Baines, C.; Shimizu, Y.; Kanoda, K.; Watanabe, I.; Saito, G. Magnetic and non-magnetic phases of a quantum spin liquid. *Nature* **2011**, *471*, 612.

(9) Jiang, H.; Yao, H.; Balents, L. Spin liquid ground state of the spin-1/2 square J_1 - J_2 Heisenberg model. *Phys. Rev. B: Condens. Matter Mater. Phys.* **2012**, *86*, 024424.

(10) Knolle, J.; Kovrizhin, D. L.; Chalker, J. T.; Moessner, R. Dynamics of a two-dimensional quantum spin liquid: signatures of emergent Majorana fermions and fluxes. *Phys. Rev. Lett.* **2014**, *112*, 207203.

(11) Wilczek, F. Majorana returns. *Nat. Phys.* **2009**, *5*, 614–618.

(12) Ross, K. A.; Savary, L.; Gaulin, B. D.; Balents, L. Quantum excitations in quantum spin ice. *Phys. Rev. X* **2011**, *1*, 021002.

(13) Witczak-Krempa, W.; Chen, G.; Kim, Y.; Balents, L. Correlated quantum phenomena in the strong spin-orbit regime. *Annu. Rev. Condens. Matter Phys.* **2014**, *5*, 57–82.

(14) Petit, S.; Lhotel, E.; Canals, B.; Ciomaga Hatnean, M.; Ollivier, J.; Mutka, H.; Ressouche, E.; Wildes, A. R.; Lees, M. R.; Balakrishnan, G. Observation of magnetic fragmentation in spin ice. *Nat. Phys.* **2016**, *12*, 746–750.

(15) Khomskii, D. I. Electric dipoles on magnetic monopoles in spin ice. *Nat. Commun.* **2012**, *3*, 904.

(16) Brooks-Bartlett, M. E.; Banks, S. T.; Jaubert, L. D. C.; Harman-Clarke, A.; Holdsworth, P. C. W. Magnetic-moment fragmentation and monopole crystallization. *Phys. Rev. X* **2014**, *4*, 011007.

(17) Wan, X.; Turner, A. M.; Vishwanath, A.; Savrasov, S. Y. Topological semimetal and Fermi-arc surface states in the electronic structure of pyrochlore iridates. *Phys. Rev. B: Condens. Matter Mater. Phys.* **2011**, *83*, 205101.

(18) Iqbal, Y.; Muller, T.; Ghosh, P.; Gingras, M. J. P.; Jeschke, H. O.; Rachel, S.; Reuther, J.; Thomale, R. Quantum and classical phases of the pyrochlore Heisenberg model with competing interactions. *Phys. Rev. X* **2019**, *9*, 011005.

(19) Powell, B. J.; Mckenzie, R. H. Quantum frustration in organic Mott insulators: from spin liquids to unconventional superconductors. *Rep. Prog. Phys.* **2011**, *74*, 056501.

(20) Ding, L.; Manuel, P.; Bachus, S.; Grußler, F.; Gegenwart, P.; Singleton, J.; Johnson, R. D.; Walker, H. C.; Adroja, D. T.; Hillier, A. D.; Tsirlin, A. A. Gapless spin-liquid state in the structurally disorder-free triangular antiferromagnet NaYbO_2 . *Phys. Rev. B: Condens. Matter Mater. Phys.* **2019**, *100*, 144432.

(21) Li, Y.; Chen, G.; Tong, W.; Pi, L.; Liu, J.; Yang, Z.; Wang, X.; Zhang, Q. Rare-earth triangular lattice spin liquid: a single-crystal study of YbMgGaO_4 . *Phys. Rev. Lett.* **2015**, *115*, 167203.

(22) Paddison, J. A. M.; Daum, M.; Dun, Z.; Ehlers, G.; Liu, Y.; Stone, M. B.; Zhou, H.; Mourigal, M. Unconventional quantum Hall effect and Berry's phase of 2π in bilayer graphene. *Nat. Phys.* **2017**, *13*, 117–122.

(23) Shen, Y.; Li, Y.; Wo, H.; Li, Y.; Shen, S.; Pan, B.; Wang, Q.; Walker, H. C.; Steffens, P.; Boehm, M.; Hao, Y.; Quintero-Castro, D. L.; Harriger, L. W.; Frontzek, M. D.; Hao, L.; Meng, S.; Zhang, Q.; Chen, G.; Zhao, J. Evidence for a spinon Fermi surface in a triangular-lattice quantum-spin-liquid candidate. *Nature* **2016**, *540*, 559–562.

(24) Balents, L. Spin liquids in frustrated magnets. *Nature* **2010**, *464*, 199–208.

(25) Zhou, Y.; Kanoda, K.; Ng, T. Quantum spin liquid states. *Rev. Mod. Phys.* **2017**, *89*, 025003.

(26) “Quantum spin liquids and fractionalization” in *Introduction to frustrated magnetism*; Misguich, G., Lacroix, C., Mendels, P., Mila, F., Eds.; Springer: Berlin, 2011.

(27) Imai, T.; Lee, Y. S. Do quantum spin liquids exist? *Phys. Today* **2016**, *69*, 30.

(28) Lee, P. A. An end to the drought of quantum spin liquids. *Science* **2008**, *321*, 1306.

(29) Norman, M. R. Colloquium: Herbertsmithite and the search for the quantum spin liquid. *Rev. Mod. Phys.* **2016**, *88*, 041002.

(30) Savary, L.; Balents, L. Quantum spin liquids: a review. *Rep. Prog. Phys.* **2017**, *80*, 016502.

(31) Broholm, C.; Cava, R. J.; Kivelson, S. A.; Nocera, D. G.; Norman, M. R.; Senthil, T. Quantum spin liquids. *Science* **2020**, *367*, eaay0668.

- (32) Takagi, H.; Takayama, T.; Jackeli, G.; Khaliullin, G.; Nagler, S. E. Concept and realization of Kitaev quantum spin liquids. *Nat. Rev. Phys.* **2019**, *1*, 264–280.
- (33) Wen, J.; Yu, S.; Li, S.; Yu, W.; Li, J. Experimental identification of quantum spin liquids. *npj Quantum Mater.* **2019**, *4*, 12.
- (34) Mila, F. Quantum spin liquids. *Eur. J. Phys.* **2000**, *21*, 499–510.
- (35) Schlom, D.; Chen, L.; Eom, C.; Rabe, K.; Streiffer, S.; Triscone, J. Strain Tuning of ferroelectric thin films. *Annu. Rev. Mater. Res.* **2007**, *37*, 589–626.
- (36) Zubko, P.; Gariglio, S.; Gabay, M.; Ghosez, P.; Triscone, J. Interface physics in complex oxide heterostructures. *Annu. Rev. Condens. Matter Phys.* **2011**, *2*, 141–65.
- (37) Hwang, H. Y.; Iwasa, Y.; Kawasaki, M.; Keimer, B.; Nagaosa, N.; Tokura, Y. Emergent phenomena at oxide interfaces. *Nat. Mater.* **2012**, *11*, 103–113.
- (38) Chakhalian, J.; Freeland, J. W.; Millis, A. J.; Panagopoulos, C.; Rondinelli, J. M. Colloquium: Emergent properties in plane view: Strong correlations at oxide interfaces. *Rev. Mod. Phys.* **2014**, *86*, 1189.
- (39) Stemmer, S.; James Allen, S. Two-dimensional electron gases at complex oxide interfaces. *Annu. Rev. Mater. Res.* **2014**, *44*, 151–71.
- (40) Huang, Z.; Ariando; Renshaw Wang, X.; Rusydi, A.; Chen, J.; Yang, H.; Venkatesan, T. Interface engineering and emergent phenomena in oxide heterostructures. *Adv. Mater.* **2018**, *30*, 1802439.
- (41) Ramesh, R.; Schlom, D. Creating emergent phenomena in oxide superlattices. *Nat. Rev. Mater.* **2019**, *4*, 257–268.
- (42) Ueda, K.; Tabata, H.; Kawai, T. Ferromagnetism in LaFeO₃-LaCrO₃ superlattices. *Science* **1998**, *280*, 1064.
- (43) Gibert, M.; Zubko, P.; Scherwitzl, R.; Iniguez, J.; Triscone, J. Exchange bias in LaNiO₃-LaMnO₃ superlattices. *Nat. Mater.* **2012**, *11*, 195.
- (44) Liu, X.; Middey, S.; Cao, Y.; Kareev, M.; Chakhalian, J. Geometrical lattice engineering of complex oxide heterostructures: a designer approach to emergent quantum states. *MRS Commun.* **2016**, *6*, 133–144.
- (45) Middey, S.; Meyers, D.; Doennig, D.; Kareev, M.; Liu, X.; Cao, Y.; Yang, Z.; Shi, J.; Gu, L.; Ryan, P. J.; Pentcheva, R.; Freeland, J. W.; Chakhalian, J. Mott electrons in an artificially graphenelike crystal of rare-earth nickelate. *Phys. Rev. Lett.* **2016**, *116*, 056801.
- (46) Kim, T. H.; Puggioni, D.; Yuan, Y.; Xie, L.; Zhou, H.; Campbell, N.; Ryan, P. J.; Choi, Y.; Kim, J.-W.; Patzner, J. R.; Ryu, S.; Podkaminer, J. P.; Irwin, J.; Ma, Y.; Fennie, C. J.; Rzchowski, M. S.; Pan, X. Q.; Gopalan, V.; Rondinelli, J. M.; Eom, C. B. Polar metals by geometric design. *Nature* **2016**, *533*, 68–72.
- (47) Arab, A.; Liu, X.; Köksal, O.; Yang, W.; Chandrasena, R.; Middey, S.; Kareev, M.; Kumar, S.; Husanu, M.; Yang, Z.; Gu, L.; Strocov, V.; Lee, T.; Minar, J.; Pentcheva, R.; Chakhalian, J.; Gray, A. X. Electronic structure of a graphenelike artificial crystal of NdNiO₃. *Nano Lett.* **2019**, *19*, 8311–8317.
- (48) Liu, X.; Singh, S.; Kirby, B. J.; Zhong, Z.; Cao, Y.; Pal, B.; Kareev, M.; Middey, S.; Freeland, J. W.; Shafer, P.; Arenholz, E.; Vanderbilt, D.; Chakhalian, J. Emergent magnetic state in (111)-oriented quasi-two-dimensional spinel oxides. *Nano Lett.* **2019**, *19*, 8381–8387.
- (49) Xu, C.; Feng, J.; Kawamura, M.; Yamaji, Y.; Nahas, Y.; Prokhorenko, S.; Qi, Y.; Xiang, H.; Bellaiche, L. Possible Kitaev quantum spin liquid state in 2D materials with $S = 3/2$. *Phys. Rev. Lett.* **2020**, *124*, 087205.
- (50) Koga, A.; Minakawa, T.; Murakami, Y.; Nasu, J. Spin transport in the quantum spin liquid state in the $S = 1$ Kitaev model: Role of the fractionalized quasiparticles. *J. Phys. Soc. Jpn.* **2020**, *89*, 033701.
- (51) Lee, H.; Kawashima, N.; Kim, Y. Tensor network wave function of $S = 1$ Kitaev spin liquids. *Phys. Rev. Research* **2020**, *2*, 033318.
- (52) Mufti, N.; Nugroho, A. A.; Blake, G. R.; Palstra, T. T. M. Magnetodielectric coupling in frustrated spin systems: the spinels MCr₂O₄ (M = Mn, Co and Ni). *J. Phys.: Condens. Matter* **2010**, *22*, 075902.
- (53) Lyons, D. H.; Kaplan, T. A.; Dwight, K.; Menyuk, N. Classical theory of the ground spin-state in cubic spinels. *Phys. Rev.* **1962**, *126*, 540.
- (54) Tomiyasu, K.; Fukunaga, J.; Suzuki, K. Magnetic short-range order and reentrant-spin-glass-like behavior in CoCr₂O₄ and MnCr₂O₄ by means of neutron scattering and magnetization measurements. *Phys. Rev. B: Condens. Matter Mater. Phys.* **2004**, *70*, 214434.
- (55) Chang, L.; Huang, D.; Li, W.-H.; Cheong, S.-W.; Ratcliff, W.; Lynn, J. Crossover from incommensurate to commensurate magnetic orderings in CoCr₂O₄. *J. Phys.: Condens. Matter* **2009**, *21*, 456008.
- (56) Liu, X.; Kareev, M.; Cao, Y.; Liu, J.; Middey, S.; Meyers, D.; Freeland, J. W.; Chakhalian, J. Electronic and magnetic properties of (111)-oriented CoCr₂O₄ epitaxial thin film. *Appl. Phys. Lett.* **2014**, *105*, 042401.
- (57) Liu, X.; Choudhury, D.; Cao, Y.; Middey, S.; Kareev, M.; Meyers, D.; Kim, J.-W.; Ryan, P.; Chakhalian, J. Epitaxial growth of (111)-oriented spinel CoCr₂O₄/Al₂O₃ heterostructures. *Appl. Phys. Lett.* **2015**, *106*, 071603.
- (58) Chen, C. T.; Idzerda, Y. U.; Lin, H.-J.; Smith, N. V.; Meigs, G.; Chaban, E.; Ho, G. H.; Pellegrin, E.; Sette, F. Experimental confirmation of the x-ray magnetic circular dichroism sum rules for iron and cobalt. *Phys. Rev. Lett.* **1995**, *75*, 152.
- (59) Yamasaki, Y.; Miyasaka, S.; Kaneko, Y.; He, J.-P.; Arima, T.; Tokura, Y. Magnetic reversal of the ferroelectric polarization in a multiferroic spinel oxide. *Phys. Rev. Lett.* **2006**, *96*, 207204.
- (60) Li, L.; Checkelsky, J. G.; Hor, Y. S.; Uher, C.; Hebard, A. F.; Cava, R. J.; Ong, N. P. Phase transitions of Dirac electrons in bismuth. *Science* **2008**, *321*, 547–550.
- (61) Li, L.; Richter, C.; Mannhart, J.; Ashoori, R. C. Coexistence of magnetic order and two-dimensional superconductivity at LaAlO₃/SrTiO₃ interfaces. *Nat. Phys.* **2011**, *7*, 762–766.
- (62) Petit, D.; Fruchter, L.; Campbell, I. A. Ordering in a spin glass under applied magnetic field. *Phys. Rev. Lett.* **1999**, *83*, 5130.
- (63) Tsurkan, V.; Zherlitsyn, S.; Yasin, S.; Felea, V.; Skourski, Y.; Deisenhofer, J.; Krug von Nidda, H.-A.; Wosnitza, J.; Loidl, A. Unconventional magnetostructural transition in CoCr₂O₄ at high magnetic field. *Phys. Rev. Lett.* **2013**, *110*, 115502.
- (64) Watanabe, D.; Yamashita, M.; Tonegawa, S.; Oshima, Y.; Yamamoto, H. M.; Kato, R.; Sheikin, I.; Behnia, K.; Terashima, T.; Uji, S.; Shibauchi, T.; Matsuda, Y. Novel Pauli-paramagnetic quantum phase in a Mott insulator. *Nat. Commun.* **2012**, *3*, 1090.
- (65) Hayano, R. S.; Uemura, Y. J.; Imazato, J.; Nishida, N.; Yamazaki, T.; Kubo, R. Zero-and low-field spin relaxation studied by positive muons. *Phys. Rev. B: Condens. Matter Mater. Phys.* **1979**, *20*, 850.
- (66) Dalmas de Reotier, P.; Yaouanc, A. Muon spin rotation and relaxation in magnetic materials. *J. Phys.: Condens. Matter* **1997**, *9*, 9113–9166.
- (67) Klanjsek, M.; Zorko, A.; Zitko, R.; Mravlje, J.; Jaglicic, Z.; Biswas, P.; Prelovsek, P.; Mihailovic, D.; Arcon, D. A high-temperature quantum spin liquid with polaron spins. *Nat. Phys.* **2017**, *13*, 1130.
- (68) Uemura, Y. J.; Yamazaki, T.; Harshman, D. R.; Senba, M.; Ansaldi, E. J. Muon-spin relaxation in AuFe and CuMn spin glasses. *Phys. Rev. B: Condens. Matter Mater. Phys.* **1985**, *31*, 546.
- (69) Li, Y.; Adroja, D.; Biswas, P. K.; Baker, P. J.; Zhang, Q.; Liu, J.; Tsirlin, A. A.; Gegenwart, P.; Zhang, Q. Muon spin relaxation evidence for the U(1) quantum spin-liquid ground state in the triangular antiferromagnet YbMgGaO₄. *Phys. Rev. Lett.* **2016**, *117*, 097201.
- (70) Luke, G. M.; Keren, A.; Le, L. P.; Wu, W. D.; Uemura, Y. J.; Bonn, D. A.; Taillefer, L.; Garrett, J. D. Muon spin relaxation in UPt₃. *Phys. Rev. Lett.* **1993**, *71*, 1466.
- (71) Chang, L.; Lees, M.; Watanabe, I.; Hillier, A.; Yasui, Y.; Onoda, S. Static magnetic moments revealed by muon spin relaxation and thermodynamic measurements in the quantum spin ice Yb₂Ti₂O₇. *Phys. Rev. B: Condens. Matter Mater. Phys.* **2014**, *89*, 184416.
- (72) Clark, L.; Orain, J. C.; Bert, F.; de Vries, M. A.; Aidoudi, F. H.; Morris, R. E.; Lightfoot, P.; Lord, J. S.; Telling, M. T. F.; Bonville, P.; Attfield, J. P.; Mendels, P.; Harrison, A. Gapless spin liquid ground

state in the $S = 1/2$ vanadium oxyfluoride kagome antiferromagnet $[\text{NH}_4]_2[\text{C}_7\text{H}_{14}\text{N}][\text{V}_7\text{O}_6\text{F}_8]$. *Phys. Rev. Lett.* **2013**, *110*, 207208.

(73) Phillips, J. C. Stretched exponential relaxation in molecular and electronic glasses. *Rep. Prog. Phys.* **1996**, *59*, 1133–1207.

(74) Uemura, Y. J.; Yamazaki, T.; Hayano, R. S.; Nakai, R.; Huang, C. Y. Zero-field spin relaxation of μ^+ as a probe of the spin dynamics of AuFe and CuMn spin-glasses. *Phys. Rev. Lett.* **1980**, *45*, 583–587.

(75) Rovers, M. T.; Kyriakou, P. P.; Dabkowska, H. A.; Luke, G. M.; Larkin, M. I.; Savici, A. T. Muon-spin-relaxation investigation of the spin dynamics of geometrically frustrated chromium spinels. *Phys. Rev. B: Condens. Matter Mater. Phys.* **2002**, *66*, 174434.

(76) Keren, A.; Kojima, K.; Le, L. P.; Luke, G. M.; Wu, W. D.; Uemura, Y. J.; Takano, M.; Dabkowska, H.; Gingras, M. J. P. Muon-spin-rotation measurements in the kagome lattice systems: Cr-jarosite and Fe-jarosite. *Phys. Rev. B: Condens. Matter Mater. Phys.* **1996**, *53*, 6451.

(77) Uemura, Y. J.; Keren, A.; Kojima, K.; Le, L. P.; Luke, G. M.; Wu, W. D.; Ajiro, Y.; Asano, T.; Kuriyama, Y.; Mekata, M.; Kikuchi, H.; Kakurai, K. Spin fluctuations in frustrated kagome lattice system $\text{SrCr}_8\text{Ga}_4\text{O}_{19}$ studied by muon spin relaxation. *Phys. Rev. Lett.* **1994**, *73*, 3306.

(78) Mendels, P.; Bert, F.; de Vries, M. A.; Olariu, A.; Harrison, A.; Duc, F.; Trombe, J. C.; Lord, J. S.; Amato, A.; Baines, C. Quantum magnetism in the paratacamite family: towards an ideal kagome lattice. *Phys. Rev. Lett.* **2007**, *98*, 077204.

(79) Quilliam, J. A.; Bert, F.; Manseau, A.; Darie, C.; Guillot-Deudon, C.; Payen, C.; Baines, C.; Amato, A.; Mendels, P. Gapless quantum spin liquid ground state in the spin-1 antiferromagnet $6\text{HBa}_3\text{NiSb}_2\text{O}_9$. *Phys. Rev. B: Condens. Matter Mater. Phys.* **2016**, *93*, 214432.

(80) Balz, C.; Lake, B.; Reuther, J.; Luetkens, H.; Schonemann, R.; Herrmannsdorfer, T.; Singh, Y.; Nazmul Islam, A.; Wheeler, E.; Rodriguez-Rivera, J.; Guidi, T.; Simeoni, G.; Baines, C.; Ryll, H. Physical realization of a quantum spin liquid based on a complex frustration mechanism. *Nat. Phys.* **2016**, *12*, 942–949.

(81) Mustonen, O.; Vasala, S.; Sadrollahi, E.; Schmidt, K. P.; Baines, C.; Walker, H. C.; Terasaki, I.; Litterst, F. J.; Baggio-Saitovitch, E.; Karppinen, M. Spin-liquid-like state in a spin-1/2 square-lattice antiferromagnet perovskite induced by $d^{10}-d^0$ cation mixing. *Nat. Commun.* **2018**, *9*, 1085.

(82) Vojta, M. Frustration and quantum criticality. *Rep. Prog. Phys.* **2018**, *81*, 064501.

Supporting Information: Proximate quantum spin liquid on designer lattice

Xiaoran Liu,^{*,†} Sobhit Singh,[†] Victor Drouin-Touchette,[†] Tomoya Asaba,[‡] Jess Brewer,^{¶,§} Qinghua Zhang,^{||} Yanwei Cao,[⊥] Banabir Pal,^{†,#} Srimanta Middey,[@] P. S. Anil Kumar,[@] Mikhail Kareev,[†] Lin Gu,^{||} D. D. Sarma,[#] Padraic Shafer,[△] Elke Arenholz,[△] John W. Freeland,[▽] Lu Li,[‡] David Vanderbilt,[†] and Jak Chakhalian[†]

[†]*Department of Physics and Astronomy, Rutgers University, Piscataway, New Jersey 08854, USA*

[‡]*Department of Physics, University of Michigan, Ann Arbor, Michigan 48109, USA*

[¶]*TRIUMF, 4004 Wesbrook Mall, Vancouver, British Columbia, Canada V6T 2A3*

[§]*Department of Physics and Astronomy, University of British Columbia, Vancouver, British Columbia, Canada V6T 1Z1*

^{||}*Beijing National Laboratory for Condensed-Matter Physics and Institute of Physics, Chinese Academy of Sciences, Beijing 100190, P. R. China*

[⊥]*Ningbo Institute of Materials Technology and Engineering, Chinese Academy of Sciences, Ningbo, Zhejiang 315201, China*

[#]*Solid State and Structural Chemistry Unit, Indian Institute of Science, Bengaluru 560012, India*

[@]*Department of Physics, Indian Institute of Science, Bengaluru 560012, India*

[△]*Advanced Light Source, Lawrence Berkley National Laboratory, Berkeley, California 94720, USA*

[▽]*Advanced Photon Source, Argonne National Laboratory, Argonne, Illinois 60439, USA*

E-mail: xiaoran.liu@rutgers.edu

Sample Fabrications

The $[n$ QL CoCr₂O₄/1.3 nm Al₂O₃]₄ ($n = 1, 2, 4$; 1 QL $\approx 4.8 \text{ \AA}$) superlattices were grown on 5 \times 5 mm² Al₂O₃ (0001) substrates by pulsed laser deposition. Stoichiometric CoCr₂O₄ and Al₂O₃ targets were ablated using a KrF excimer laser ($\lambda = 248 \text{ nm}$, energy density $\sim 2 \text{ J/cm}^2$) with a repetition rate of 4 Hz and 2 Hz, respectively. The depositions were carried out at a substrate temperature of 700 °C, under oxygen partial pressure of 5 mTorr. The films were post-annealed at the growth condition for 15 minutes and then cooled down to room temperature at 10 °C/min. The deposition process was monitored by *in-situ* high pressure reflection-high-energy-electron-diffraction (RHEED). Furthermore, quality of the superlattices has been verified by using a variety of *ex-situ* characterization methods including synchrotron-based x-ray diffraction, x-ray reflectivity, x-ray photoemission spectroscopy and atomic force microscopy, as published elsewhere.^{1,2}

DC Magnetization

In order to probe the critical temperature T_c of the magnetic phase transition, we have also investigated the temperature dependence of the *dc* magnetization on each sample (see Supplemental Fig. S1). The measurements were performed using the Quantum Design MPMS SQUID magnetometer. As shown on the graph, the para- to ferri- magnetic transition still takes place at $T_C \sim 58 \text{ K}$ on $n = 4$ and $\sim 40 \text{ K}$ on $n = 2$, respectively, whereas no clear signature of any transition was detected on the $n = 1$ sample down to 2 K.

Resonant X-ray Absorption Spectra

The local chemical states and environments of both Co and Cr cations of each sample were explored by measuring the resonant X-ray absorption Spectra (XAS). The experiments were performed at the beamline 4-ID-C of the Advanced Photon Source in Argonne National Laboratory. As shown in Supplemental Fig. S2, no signs of cation distribution disorder or variation of ion

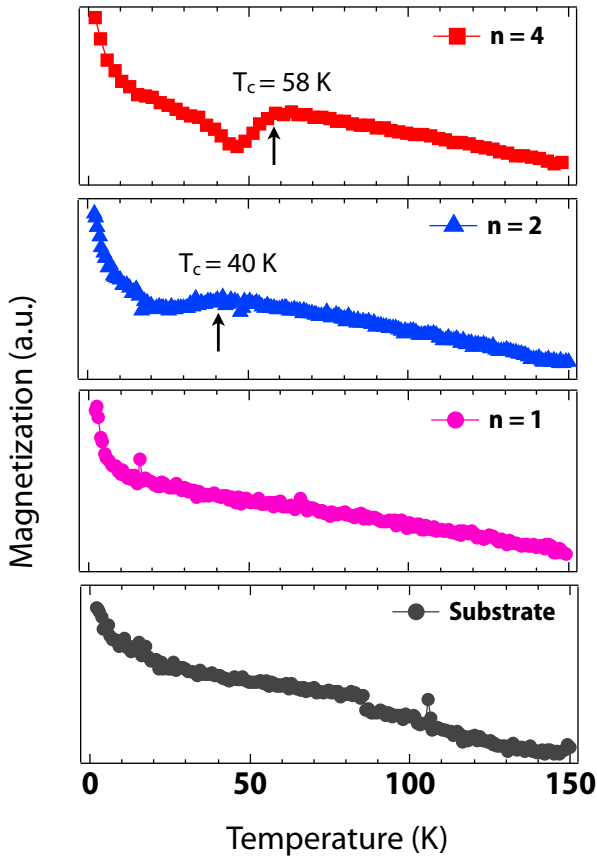


Figure S1: Temperature dependence of magnetization of $[n \text{ QL } \text{CoCr}_2\text{O}_4/1.3 \text{ nm Al}_2\text{O}_3]_4$ ($n = 1, 2, 4$), together with a bare Al_2O_3 substrate for comparison.

valency were observed for all samples as deduced from the absorption line-shapes as well as the absorption peak positions at each $L_{2,3}$ absorption edge, which are practically identical to the bulk references (i.e., all of the Co ions are tetrahedrally coordinated with +2 valency, while all Cr ions are octahedrally coordinated with +3 valency). These measurements corroborate the formation of the expected ionic layers as described in the main text.

X-ray Magnetic Circular Dichroism

X-ray magnetic circular dichroism (XMCD) spectra under 3 T external field were performed at the beamline 4-ID-C of the Advanced Photon Source in Argonne National Laboratory. The $L_{2,3}$ -edge X-ray absorption spectra of both Co and Cr were scanned with left- and right- polarized X-rays at

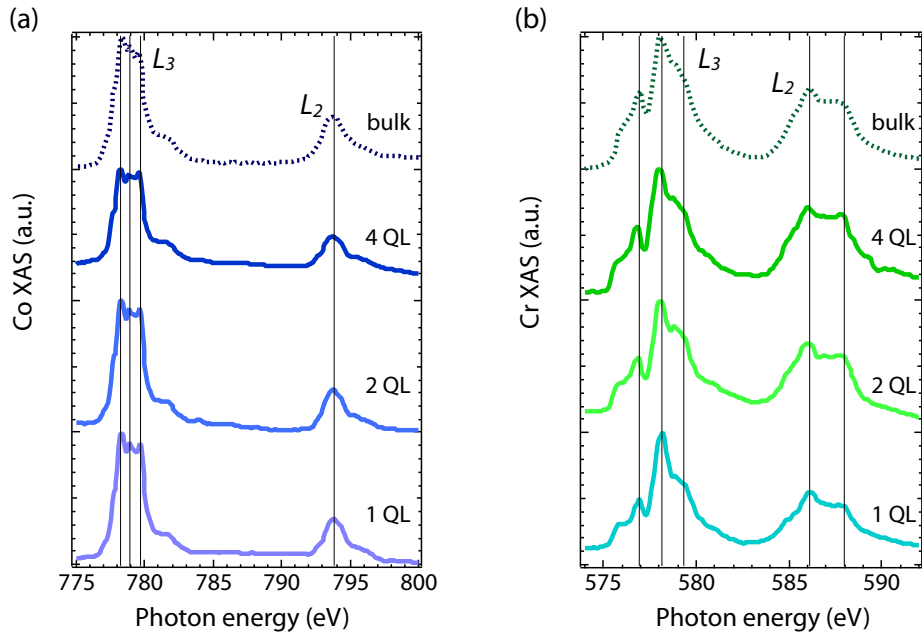


Figure S2: (a) Co and (b) Cr L_{2,3}-edges x-ray absorption spectra of the superlattices with $n = 4$, 2, and 1. Data were collected in the total electron yield (TEY) mode at 10 K. The spectra taken from measurements on bulk CoCr₂O₄ powders³ are plotted in dashed lines as references.

grazing incidence at 10 K. To exclude any artifact, all the measurements were conducted in both positive and negative external field. Data were recorded simultaneously with total electron yield (TEY), fluorescence yield (FY), and reflectivity detection modes.

The XMCD hysteresis loops were measured at the beamline 4.0.2 of the Advanced Light Source in Lawrence Berkeley National Laboratory. Samples were cooled with zero field and maintained at 15 K. The circularly polarized soft X-rays were incident with an angle of 35° relative to the sample surface. The luminescence detection mode was used to record the data.

Torque Magnetometry Measurements

Torque magnetometry measurements were performed with home-built cantilever setup by attaching samples to a thin beryllium copper cantilever. External magnetic field was applied, and the sample rotation by torque was measured by tracking the capacitance change between the metallic cantilever and a fixed gold film underneath using an AH2700A capacitance bridge with a 14

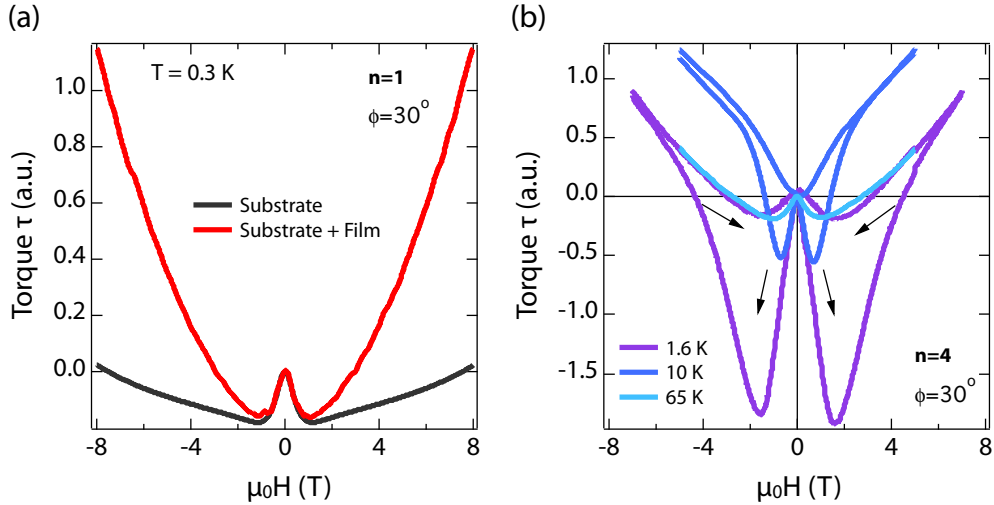


Figure S3: (a) Torque magnetometry curves of both the bare Al_2O_3 substrate (black) and the $n = 1$ sample (red) at 0.3 K. (b) Torque magnetometry curves of the $n = 4$ sample ($T_C \sim 58$ K) at 1.6 K, 10 K, and 65 K.

kHz driving frequency. To calibrate the spring constant of the cantilever, we tracked the angular dependence of capacitance caused by the sample weight at zero magnetic field.

As discussed in the main text, the torque signal from the pure film is calculated by subtracting the substrate contribution at each temperature below 30 K. Here in Supplemental Fig. S3(a), we show one set of the representative measurement performed at 0.3 K. The geometry of the setup is identical to that described in the main text. Note, the substrate was treated using the same thermal process as growing the film. As clearly seen, there is no observable magnetic hysteresis and the "bump" near zero field regime is from the substrate.

Compared to the behavior of $n = 1$, the torque data of $n = 4$ reveal remarkable distinction, as displayed in Supplemental Fig. S3(b). Above $T_C \sim 58$ K, no hysteresis loop is seen, whereas below T_C , distinct loops are observed. These measurements are consistent with results from SQUID and XMCD, providing another solid evidence on the establishment of long-range ferrimagnetic ordering in $n = 4$, which in addition highlights the particularity of $n = 1$.

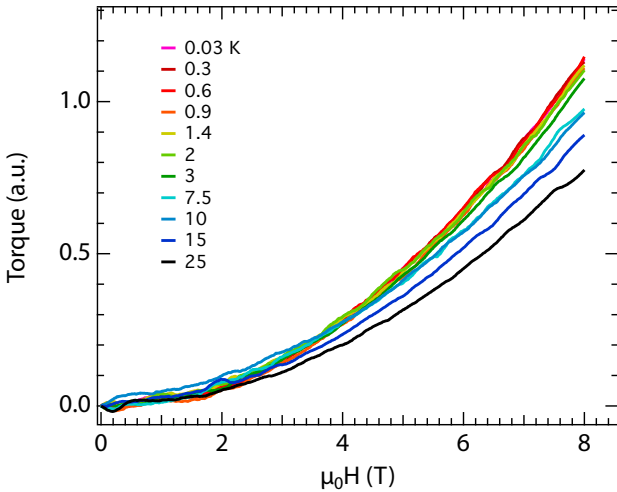


Figure S4: Torque magnetometry curves as a function of field of the 1 QL CoCr_2O_4 system between 30 – 0.03 K.

Muon Spin Relaxation Spectra

Positive muon spin relaxation ($\mu^+\text{SR}$) experiments were carried out in both zero magnetic field (ZF) and a 30 G weak transverse field (wTF) on the LEM (Low-Energy Muon) spectrometer at PSI (the Paul Scherrer Institut) in Switzerland. Five identical pieces of the $n = 1$ samples on Al_2O_3 substrate were mounted on a nickel backing in order to completely depolarize any muons missing the samples. Thanks to the momentum dispersion introduced by passage through the thin carbon foil that produces free electrons to trigger the incoming muon counter, the time of flight from that foil to the sample is broadened, causing a reduced time resolution and a distorted decay spectrum over the first $\sim 0.2 \mu\text{s}$. Oscillations faster than about 10 MHz (corresponding to local fields of over ~ 70 mT) cannot be resolved. The measurements were performed at a set of temperatures in the range of 4 - 100 K, exhibiting similar behaviors. In particular, no oscillatory signal is observed in any of the ZF- $\mu^+\text{SR}$ spectra down to and including 4 K, while a slowly relaxing signal precessing at the muon Larmor frequency is clearly observed in all of the wTF- $\mu^+\text{SR}$ spectra. The spectra of both ZF- $\mu^+\text{SR}$ and wTF- $\mu^+\text{SR}$ at each temperature with fitting are shown in Supplemental Fig. S5.

The wTF- and ZF- $\mu^+\text{SR}$ time spectra were fit simultaneously with a common slowly-relaxing

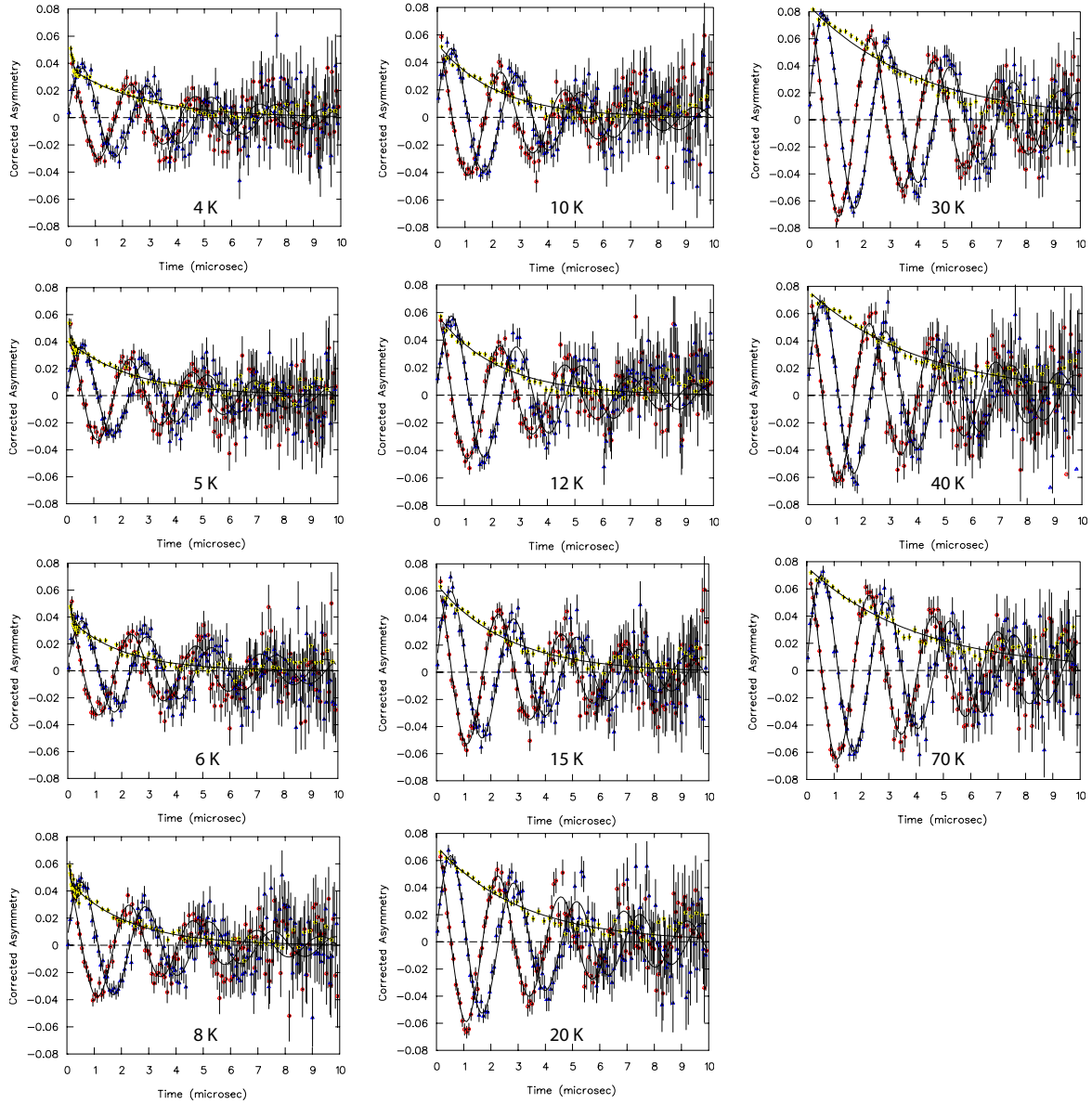


Figure S5: Spectra of the time evolution of muon-spin polarization in both zero-field (ZF, yellow stars) and 30 G transverse field (TF, red circles [real part] and blue triangles [imaginary part]) at 11 temperatures within 4 - 70 K. The spectra measured at these temperatures were fit using the equations as discussed in the text.

asymmetry A_{slow} but all other parameters independent. At temperatures below 10 K, an additional fast-relaxing component was apparent in the ZF spectra, but not in the wTF spectra. We believe this to be due to the systematic leakage of uncorrelated beam particles, and so the fast-relaxing asymmetry reveals no physical information about the sample. Simple exponential relaxation was assumed throughout, as fits with more exotic relaxation shapes were not appreciably better. Thus the ZF- μ^+ SR data below 10 K were fit with the sum of a fast exponential relaxation and a slow exponential relaxation:

$$A_0 P_{\text{ZF}}(t) = A_{\text{fast}} e^{-\lambda_{\text{fast}} t} + A_{\text{slow}} e^{-\lambda_{\text{ZF}} t}$$

in which A_0 is the overall initial asymmetry and $P_{\text{ZF}}(t)$ is the muon spin-polarization relaxation function. The asymmetries (A_{fast} , A_{slow}) and the slow relaxation rate (λ_{ZF}) are the important fitting parameters. The slow terms (A_{slow} and λ_{ZF}) are related to the actual muon spin relaxation inside the sample, which are the subjects of interest. At the same time, the wTF- μ^+ SR data was fit to a single exponentially relaxing precession at the frequency corresponding to the applied field:

$$A_0 P_{\text{wTF}}(t) = A_{\text{slow}} e^{-\lambda_{\text{TF}} t} \cos(\omega_\mu t + \phi)$$

in which ω_μ is the muon Larmor frequency ($\omega_\mu = \gamma_\mu H$, $\gamma_\mu = 2\pi \times 135.54$ MHz/T), and ϕ is the initial phase of precession. These, the asymmetry A_{slow} and the relaxation rate λ_{TF} are the important fitting parameters.

The temperature dependence of the common slow asymmetry (A_{slow}) and both relaxation rates (λ_{ZF} and λ_{TF}) are plotted in Fig. S6, showing a consistent trend. While the asymmetry decreases at low temperature, both relaxation rates first increase, reaching a “peak” at around 9-10 K, followed by a reduction again at lower temperatures. The ZF relaxation rate is consistently about twice as fast as the TF relaxation rate at the same temperature.

In addition to runs with a muon energy of 2 keV (optimizing the muon range in the middle of the film) a separate set of runs at 10 keV were taken to probe the Al₂O₃ substrate. The signal amplitude in the latter runs was found to *increase* at low temperature, unlike that in the superlattice,

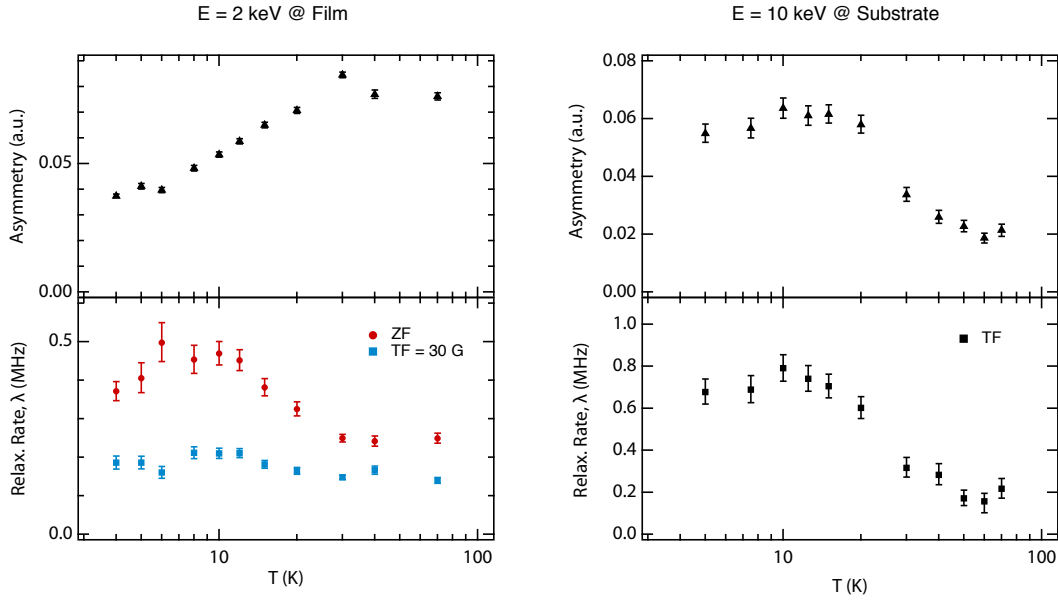


Figure S6: Asymmetry and relaxation rate of both film (left) and substrate (right) as a function of temperature.

which decreases. Moreover, the relaxation rate in Al_2O_3 (which also increases with decreasing T) is more than three times as fast as in the superlattice at base temperature. The fraction of muons in the superlattice that are not immediately depolarized at base temperature therefore cannot be just those stopping in the Al_2O_3 layers, unless such thin sheets of Al_2O_3 behave completely differently from bulk Al_2O_3 .

Density-Functional Theory Calculations

Density-functional theory (DFT) based first-principles calculations were performed using the Vienna *ab initio* simulation package (VASP)^{4,5} within the projected-augmented wave (PAW) framework.^{6,7} Nine valence electrons of Co ($3d^74s^2$), twelve valence electrons of Cr ($3p^63d^54s^1$), and six valence electrons of O ($2s^22p^4$) were considered in the PAW pseudo-potentials. The generalized gradient approximation (GGA) as parametrized by Perdew-Burke-Ernzerhof (PBE)⁸ was used for the exchange-correlation functional. We use Dudarev's approach⁹ to include the effects arising due to the strongly correlated nature of $3d$ electrons at the mean-field level. The PBE+ U scheme was

employed, where $U_{Co} = 3.3$ eV and $U_{Cr} = 3.7$ eV were used for the on-site Hubbard interaction terms for the $3d$ electrons of Co and Cr. These values of Hubbard parameter are reported to correctly describe the structural phase transitions and the magnetic ground state of bulk CoCr_2O_4 .¹⁰⁻¹³ We used an $8 \times 8 \times 8$ Monkhorst-Pack type k -mesh to sample the Brillouin zone. 600 eV was set as the cutoff for the kinetic energy of plane waves. 10^{-3} eV/Å, and 10^{-8} eV was used as the convergence criteria for residual forces and total energy in the self-consistent DFT calculations, respectively. All DFT calculations were performed in collinear magnetic setting.

The structural primitive cell of CoCr_2O_4 contains two formula units of CoCr_2O_4 with a total of six magnetic cations (2 Co and 4 Cr), as shown in Fig. S7(a). The optimized lattice parameters of bulk CoCr_2O_4 are $a = b = c = 8.34$ Å, with $x = 0.26$ as an internal structural parameter for oxygen atoms in the cubic spinel structure (space group $Fd\bar{3}m$). The Co-O, Cr-O, and Cr-Cr bond lengths in the DFT optimized cell are ~ 2.00 , ~ 2.03 , and ~ 3.00 Å, respectively. Our DFT calculations, using the aforementioned parameters, predict a Neél-type magnetic configuration as the magnetic ground state of bulk CoCr_2O_4 in which all Co atoms are in a spin-up configuration ($\uparrow\uparrow$) and all Cr atoms are in a spin-down configuration ($\downarrow\downarrow\downarrow\downarrow$). The total magnetic moment of Co and Cr atoms remained around $2.7 \mu_B$ and $3.0 \mu_B$, respectively, in our DFT calculations.

To simulate a slab geometry corresponding to $n = 1$ layer, we created an epitaxial heterostructures containing 1 unit cell of CoCr_2O_4 sandwiched between a spacer layer of nonmagnetic and insulating MgAl_2O_4 , as shown in Fig. S7(b). The details of $n = 2$ heterostructure are given in Ref.¹⁶ Note, since the sole purpose here is to use a nonmagnetic material which prevents the magnetic interactions between the periodical images of CoCr_2O_4 film, we have chosen MgAl_2O_4 as the spacer material (in place of Al_2O_3) for purposes of computational simplicity and efficiency. We ensured that the thickness of the MgAl_2O_4 spacer layer is sufficient to prevent the magnetic interactions between the adjacent CoCr_2O_4 films. The $\text{CoCr}_2\text{O}_4/\text{MgAl}_2\text{O}_4$ heterostructure was optimized using the same convergence criteria as used for the bulk CoCr_2O_4 , however, a relatively smaller Monkhorst-Pack type k -mesh of size $8 \times 8 \times 6$ was used to sample the Brillouin zone. Mg ($3s^2$) and Al ($3s^23p^1$) PAW pseudo-potentials were used. This slab heterostructure geometry

is similar to the one used for our experiments.

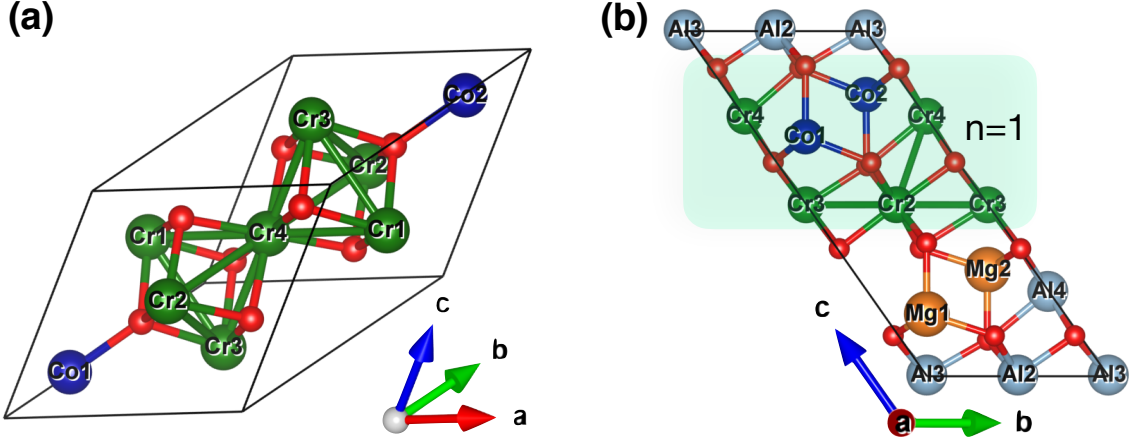


Figure S7: (a) The primitive cell of bulk CoCr_2O_4 . Red, blue, and green colors depict oxygen, cobalt and chromium atoms, respectively. (b) Side view of $n = 1$ epitaxial $\text{CoCr}_2\text{O}_4/\text{MgAl}_2\text{O}_4$ heterostructure.

Magnetic Exchange Interaction Parameters

In order to determine the magnetic exchange constants (J_{ij}) between the nearest (J_{ij}^1), and the second-near (J_{ij}^2) neighbors, we calculate the total energy of several different collinear magnetic configurations, and then project the DFT+ U calculated total energies onto the below classical Heisenberg spin model,

$$H = E_0 + \sum_{\langle i,j \rangle} J_{ij}^{(1)} \mathbf{S}_{i,A} \cdot \mathbf{S}_{j,B} + \sum_{\langle\langle i,j \rangle\rangle} J_{ij}^{(2)} \mathbf{S}_{i,A} \cdot \mathbf{S}_{j,B}. \quad (1)$$

Here, $\langle i,j \rangle$ indices refer to the nearest A (Co) and B (Cr) sublattices, whereas $\langle\langle i,j \rangle\rangle$ indices refer to the second-near neighbor A and B sublattices. $\mathbf{S}_{i,A}$ and $\mathbf{S}_{j,B}$ denote the spins at A and B magnetic sites. E_0 represents a constant energy term. A doubled unit cell was used to extract the second-neighbour magnetic exchange constants in bulk. However, for $n = 1$ $\text{CoCr}_2\text{O}_4/\text{MgAl}_2\text{O}_4$ heterostructure, only three relevant nearest-neighbor magnetic exchange constants were considered.

Figure S8 shows the fitting of our model spin Hamiltonian with the DFT+ U calculated energies

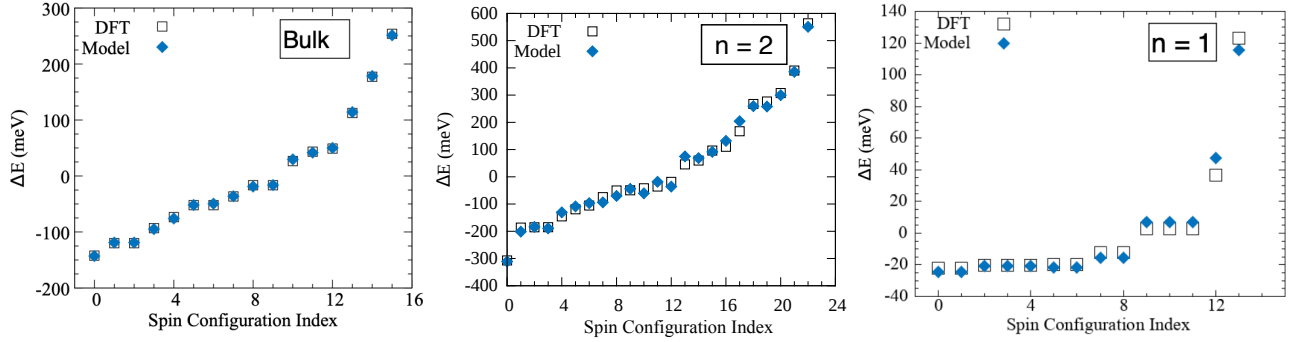


Figure S8: Fitting of the DFT+ U data with our classical Heisenberg spin model, given in Eq. 1, for bulk CoCr₂O₄, $n = 2$, and $n = 1$ slab configurations. Numerous competing magnetic ground state spin configurations can be noticed for $n = 1$ case. We note that only three relevant nearest-neighbor $J_{ij}^{(1)}$ parameters were used for fitting the $n = 1$ data, whereas five ($J_{ij}^{(1)}$ and $J_{ij}^{(2)}$) exchange coupling parameters were used to fit the bulk and $n = 2$ data, as listed in Table S1.

for bulk, $n = 2$, and $n = 1$ cases. A reasonably good fitting was obtained for all three cases, which boosts our confidence in the prediction of the fitting parameters J_{ij} . Thus obtained values of magnetic exchange parameters for bulk, $n = 2$, and $n = 1$ cases are listed in Table S1. In our model, a positive J_{ij} denotes antiferromagnetic (AFM) exchange interaction, whereas a negative J_{ij} denotes ferromagnetic (FM) exchange interaction. Our predicted nearest neighbor exchange interactions $J_{ij}^{(1)}$ for bulk CoCr₂O₄ are in good agreement with the previous reports.^{10,11,13,14}

For all three cases, the $J_{AB}^{(1)}$ is the most dominating exchange interaction (AFM) which is primarily responsible for establishing a Ne  l type AFM order in the studied systems. However, the subsequent $J_{BB}^{(1)}$ and $J_{AA}^{(1)}$ AFM terms introduce magnetic frustration at the A and B sites. We note that a larger ratio of $J_{BB}^{(1)}/J_{AB}^{(1)}$ implies the presence of strong magnetic frustrations, as suggested by the LKDM theory.¹⁵ Our analysis reveals that the $J_{BB}^{(1)}/J_{AB}^{(1)}$ ratio, which governs the magnetic frustration in this system, enhances upon the dimensional reduction [$J_{BB}^{(1)}/J_{AB}^{(1)} = 0.43$ (bulk), 0.52 ($n = 2$), and 0.98 ($n = 1$)], indicating an anomalously large enhancement in magnetic frustration for $n = 1$ case. Consequently, a distinct magnetic ground state is hard to stabilize in $n = 1$ uc thick film even at ultralow temperatures. This is consistent with our experimental results as well as with our Monte-Carlo simulations results presented below.

Here, we must note that the DFT+ U computed total energies for bulk, $n = 2$, and $n = 1$ cases

involve structures having different chemistry in regard to the total number of orbitals, total number of electrons, pseudopotentials, and interface-induced effects. Moreover, only three exchange coupling parameters [first neighbors: $J_{AA}^{(1)}$, $J_{AB}^{(1)}$, and $J_{BB}^{(1)}$] were used for fitting the DFT+ U energy data for $n = 1$ case, whereas five exchange coupling parameters [first and second neighbors: $J_{AA}^{(1)}$, $J_{AB}^{(1)}$, $J_{BB}^{(1)}$, $J_{AB}^{(2)}$, and $J_{BB}^{(2)}$] were used to fit the DFT+ U data for the bulk and $n = 2$ cases. Therefore, the absolute values of the extracted exchanges constants cannot be “assertively” compared on the same footing. However, their ratio for each systems can be compared since the ratio of the different exchange constants (*e.g.*, $J_{BB}^{(1)}/J_{AB}^{(1)}$) rules out the differences arising due to the numerical details of the DFT+ U calculations for the studied systems.

Table S1: The first-neighbor $J_{ij}^{(1)}$, and the second-neighbor $J_{ij}^{(2)}$ magnetic exchange constants (in meV units) obtained using PBE+ U for bulk CoCr₂O₄, $n = 2$, and $n = 1$ cases. Note that only three relevant first-neighbor $J_{ij}^{(1)}$ parameters were used for fitting the $n = 1$ data.

$J_{ij}^{(N)}$	bulk	$n = 2$	$n = 1$
$J_{AA}^{(1)}$	0.70	4.16	2.19
$J_{AB}^{(1)}$	4.85	12.3	4.56
$J_{BB}^{(1)}$	2.10	6.35	4.49
$J_{AB}^{(2)}$	-0.61	-1.03	—
$J_{BB}^{(2)}$	-0.04	-0.55	—
$J_{BB}^{(1)}/J_{AB}^{(1)}$	0.43	0.52	0.98

We note that $J_{AA}^{(1)}$ is the weakest first-neighbor exchange in bulk CoCr₂O₄ (corresponding Co-Co bond length = 3.66 Å), therefore, we consider the second-neighbor $J_{AA}^{(2)}$ term to be negligible due to the large Co-Co bond length (~6.0 Å) for the second-neighbour Co-Co interactions.

Notably, the second-neighbor exchange interaction terms, $J_{AB}^{(2)}$ and $J_{BB}^{(2)}$, are FM in nature, which tend to suppress the magnetic frustration arising due to the first-neighbor AFM $J_{ij}^{(1)}$. Thus, the presence of $J_{ij}^{(2)}$ terms in bulk counterbalances the magnetic frustration and facilitates a clear magnetic order (with canted spins due to the non-zero $J_{BB}^{(1)}$ and $J_{AA}^{(1)}$ terms) in the bulk. However, in the $n = 1$ slab case, the number of second-neighbor exchange interaction terms along the out-of-plane direction of film are truncated due to the presence of the nonmagnetic spacer layer. This scarcity of second-neighbor FM $J_{ij}^{(2)}$ terms, required to balance the magnetic frustration, yields

strong uncompensated magnetic frustration in the $n = 1$ slab. Due to this reason, a distinct magnetic ground state is hard to stabilize in $n = 1$ film even at ultralow temperatures (~ 30 mK in our case).

We further verify the aforementioned arguments by performing classical Monte-Carlo (MC) simulations for bulk and slab systems of CoCr_2O_4 . Our Monte-Carlo simulations show that a distinct magnetic ground state can be achieved for bulk system at low temperatures, however, there exists plenty of competing magnetic ground states for $n = 1$ and $n = 2$ unit cell thick films of CoCr_2O_4 , as discussed below.

Monte-Carlo Simulations

Finite temperature thermodynamics were obtained using a combination of parallel tempering moves^{17–20} and adaptive Metropolis steps.^{21,22} The combination of these two efficient updates led us to achieve thermalization even at very low-temperatures. Our Monte-Carlo simulations were performed using the layered cell (see figure S7 (b)), which has 2 Co spins \mathbf{S}_A and 4 Cr spins \mathbf{S}_B , first on the bulk system, using periodic boundary conditions in all directions, with $N_x = N_y = N_z = N_0$ with N_0 of at most 16 cells, and then for the slab systems having periodic boundary conditions only along in-plane x and y directions.

We used a classical Heisenberg spin model with first and second nearest neighbors between A (Co atoms) and B (Cr atoms) sites, as given by the following spin Hamiltonian:

$$\begin{aligned} H = & J_{AA}^{(1)} \sum_{\langle i,j \rangle} \mathbf{S}_{i,A} \cdot \mathbf{S}_{j,A} + J_{BB}^{(1)} \sum_{\langle i,j \rangle} \mathbf{S}_{i,B} \cdot \mathbf{S}_{j,B} \\ & + J_{BB}^{(2)} \sum_{\langle\langle i,j \rangle\rangle} \mathbf{S}_{i,B} \cdot \mathbf{S}_{j,B} \\ & + J_{AB}^{(1)} \sum_{\langle i,j \rangle} \mathbf{S}_{i,A} \cdot \mathbf{S}_{j,B} + J_{AB}^{(2)} \sum_{\langle\langle i,j \rangle\rangle} \mathbf{S}_{i,A} \cdot \mathbf{S}_{j,B} \end{aligned} \quad (2)$$

with the magnetic exchange parameters predicted by the DFT calculations (Table S1) as an input

for our Monte-Carlo simulations. Spins were considered classical since the size of the spins is $S = 3/2$, hence, quantum effects are not included in our model. However, we would like to mention that quantum effects could govern the underlying physics of this system at ultra-low temperatures. For all simulations, 30,000 MC updates per site were performed and discarded to achieve full thermalization. Another 30,000 steps were done to obtain thermodynamical observable such as energy, magnetization and specific heat. Error on obtained averages were calculated using the Jackknife method.¹⁷ At most, we ran 96 simulations in parallel at different temperatures, ranging from $T_{low} = 0.001 J_{AB}^1$ to $T_{low} = 3 J_{AB}^1$. For $J_{AB}^1 \simeq 4.85 \text{ meV} \simeq 56 K$, this corresponds to a range from $56 mK$ to $168 K$. Classical Monte-Carlo simulations at these low-temperatures are only provided in an exploratory manner, as it is quite possible that strong quantum effects become important before reaching such temperatures.

We find that the bulk system undergoes a single first-order phase transition at $T_C \simeq 85 K$. The low-temperature ordered state is a canted antiferromagnet, with $\mathbf{S}_{i,A} \cdot \mathbf{S}_{i,B} = \cos[\theta(T)]$. At $T = 0$, the system goes to $\theta = \pi$, and the Co and Cr spins are anti-aligned in the unit cell such that $\mathbf{S}_A = -\mathbf{S}_B$, which is then repeated perfectly across the system. This result can be seen in the behavior of the total magnetization $M_{tot} = \frac{1}{N} |\sum_i \sum_{j=1}^6 \mathbf{S}_{i,j}|$ with $\mathbf{S}_{i,j}$ the j -th spin of the i -th unit cell (see Fig. S9). It is also evident in the canting measure behavior. The canting measure is defined as $C_{AB} = \frac{1}{N} |\sum_i \sum_{j_A=1}^2 \sum_{j_B=3}^6 \mathbf{S}_{i,j_A} \cdot \mathbf{S}_{i,j_B}|$ (see Fig. S9), and for a perfect AF state at zero temperature, will converge to 8.

Simulations were also performed for two slab systems ($n = 1, 2$), where $N_x = N_y = N_0$ with N_0 at most 30 cells, and slab thickness $N_z = 1, 2$. Periodic boundary conditions were maintained in the x and y directions, whereas an open boundary was kept in the z direction. The unit cell was chosen in such a way that the x, y, z axes are similar to the laboratory frame, and the orientation of layers corresponds to the ones obtained via thin-film deposition (see Fig. S7(b)). For both $n = 1, 2$ slabs, we find that the canted AFM bulk state at low temperature is avoided. Although the slabs go through a phase transition at a similar temperature as the bulk $T_C^{slab} \sim 50 K$, due to the activation of dominating first-neighbor J_{AB}^1 exchange interactions, there is a big distinction between the slab and

bulk systems at low temperature. In the slab systems, a distinct magnetically ordered phase never really sets in, as evident in Figure S10, where significant energy and magnetization fluctuations are still present.

The following subsections present details on the Monte-Carlo algorithm used, and then specific measurements for the bulk and slab simulations, as well as a discussion of the thermalization.

Monte-Carlo Algorithm:

We used a combination of two algorithms. Firstly, we used a local Metropolis update, albeit modified a bit to achieve optimal sampling.^{21,22} In this method, one proceeds by randomly selecting a site i and spin S_i , and preparing a Gaussian flipped spin

$$S'_i = \frac{S_i + \Gamma_\sigma}{|S_i + \Gamma_\sigma|} \quad (3)$$

where, Γ is a randomly generated vector according to a Gaussian distribution with variance σ . This leads to a new spin S'_i that is within a solid angle of $2\pi\sigma$ of the initial spin. This new spin then leads to a new energy for the system E'_i which is compared to the initial energy E_i . According to a usual Metropolis move, this is accepted with probability $p = \exp\{-(E'_i - E_i)/T\}$. This move can be optimized at the beginning of the algorithm by calculating, for sites A and B respectively, and at all the temperatures sampled, the acceptance rate R at which such moves lead to the new spin being accepted. Then, the variance σ is modified using $\sigma' = f\sigma$ with $f = \frac{0.5}{1-R}$. Applying this method a few times before the thermalization allows us to obtain variance σ_A and σ_B that are optimal since they lead to an acceptance ratio of 50%. This usually has the effect of having very small variance at low temperature. A too large value of variance would lead to moves that depart too much from the original spin, leading to a lot of move rejections. This is optimal when most of the moves are efficient and accepted.

We ran our simulations for $M = 96$ temperatures in parallel using the parallel tempering rou-

tine. Temperatures T_i were chosen using a geometric series $T_i = T_1 R_t^{(i-1)}$ with $R_t = \left(\frac{T_M}{T_1}\right)^{1/(M-1)}$ and $T_1 = 0.001 J_{AB}^{(1)}$ and $T_M = 3 J_{AB}^{(1)}$. In a parallel tempering move, one considers whether changing the assignment of a temperature to a given configuration is preferred. Let us consider two systems $(\mathcal{S}_i, T_i, E_i)$ and $(\mathcal{S}_j, T_j, E_j)$ with i, j being two neighboring temperatures in the temperature series. Both configurations \mathcal{S}_i and \mathcal{S}_j first undergo 100 Metropolis updates per site, yielding a final energy E_i and E_j corresponding to the configuration. One then considers exchanging $T_i \leftrightarrow T_j$ based on a probability P_{ij} . One first computes $\Delta_{ij} = [(E_i - E_j)(\frac{1}{T_i} - \frac{1}{T_j})]$ and then the temperature switch is then accepted with probability $P_{ij} = \exp\{\Delta_{ij}\}$. If such a move is accepted, the spin configuration \mathcal{S}_i is now run at temperature T_j , and vice versa.

The use of parallel tempering in a Monte-Carlo algorithm has been shown to greatly improve thermalization of the sample, as well as avoiding the formation of glassy phases.^{17–20} This is achieved because configurations reach a great level of ergodicity, having a lot of opportunity to explore the large phase space of the system.

For all simulations, 30,000 MC updates per site were performed and discarded to achieve full thermalization. Another 30,000 steps were done to obtain thermodynamic observables. Error on such obtained measurements were calculated using the Jackknife method.¹⁷ Measurements that were taken were the energy per site E , the specific heat per site C_v , the sublattice and total magnetizations M_A , M_B and M_{tot} and its susceptibility χ_{tot} , as well as the canting measurement C_{AB} . Definitions of the measurement is given below, with N understood as being the total number of supercells in the system.

$$E = \frac{H}{N} \quad (4)$$

$$C_v = \frac{\langle E \rangle^2 - \langle E^2 \rangle}{NT^2} \quad (5)$$

$$M_A = \frac{1}{N} \left| \sum_i \sum_{j_A=1}^2 \mathbf{S}_{i,j_A} \right| \quad (6)$$

$$M_B = \frac{1}{N} \left| \sum_i \sum_{j_B=1}^4 \mathbf{S}_{i,j_B} \right| \quad (7)$$

$$M_{tot} = \frac{1}{N} \left| \sum_i \left(\sum_{j_A=1}^2 \mathbf{S}_{i,j_A} + \sum_{j_B=1}^4 \mathbf{S}_{i,j_B} \right) \right| \quad (8)$$

$$\chi_{tot} = \frac{\langle M_{tot} \rangle^2 - \langle M_{tot}^2 \rangle}{NT} \quad (9)$$

$$C_{AB} = \frac{1}{N} \left| \sum_i \sum_{j_A=1}^2 \sum_{j_B=1}^4 \mathbf{S}_{i,j_A} \cdot \mathbf{S}_{i,j_B} \right| \quad (10)$$

Results for the Bulk System

In this section we examine the results for our bulk simulations. These were performed on $N_x = N_y = N_z = L$ supercells, with periodic boundary conditions in each direction. Each supercell consists of 2 A sites and 4 B sites. The results are provided in Fig. S9, where we show the specific heat, magnetization, susceptibility and canting behavior for over two decades of temperature. The temperature axis is obtained using the values for the J interactions in kelvin (K), and for the specific heat and the susceptibility, we use a logarithmic axis for the temperature to accentuate the low-temperature phase.

We see that there is a very sharp transition at $T_C \simeq 85 K$ due to the activation of J_{AB}^1 , and we have $C_v^{max} \propto L^3$ behaviour. Such a scaling behaviour is a strong indicator of a first order transition. Looking at the magnetization, it is clear that the low-temperature ordered state is a canted antiferromagnet, with $\mathbf{S}_{i,A} \cdot \mathbf{S}_{i,B} = \cos \theta(T)$. The low-temperature phase has a finite and continuously varying magnetization of the A and B sublattices as well as M_{tot} , although the change

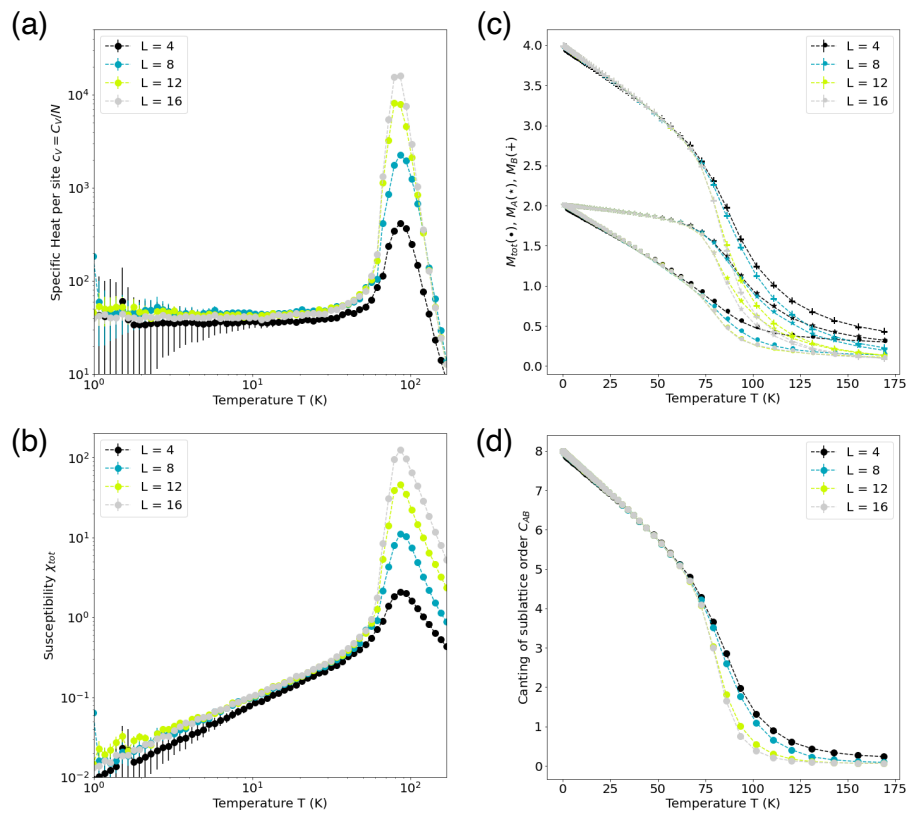


Figure S9: Thermodynamic results for the bulk simulations. Results for (a) specific heat per site, (b) susceptibility, (c) magnetization, and (d) canting angle measurements for bulk CoCr₂O₄ system.

is mainly driven by the B sites. The canted AF state can be clearly seen in the behavior of C_{AB} , which jumps from 0 to a finite value at T_C , and then progressively increases to reach a perfect AFM state at $T = 0$. This canting measure, in a state where the B sites are tilted θ degrees away from the A sites, can be equal to $C_{AB} \simeq 8|\cos\theta|$, i.e. at $T = 0$ we have a perfect AFM state. Finally, observation of the susceptibility of M_{tot} yields the same conclusions as the specific heat, and we are confident in the presence of a first-order temperature driven transition at $T_C \simeq 85 K$ to a canted AFM state in the bulk system, which is as expected from our DFT calculations.

Results for the Slab Systems

We now shift our focus to the slab simulation results. The format of the supercell used is such that stacking 2D layers in the z direction replicates the laboratory samples created by deposition. In this section, we used samples with $L_x = L_y = L$, and $L_z = 1, 2$ for the two different slabs created (mono and double layer). Periodic boundary conditions were set in the x and y directions, and open boundary in the z . In the results presented below, we used $L = 12, 16, 20$, and 30 . MC runs on smaller systems were also performed but the obtained results were too sensitive to the boundary conditions. Firstly, we present the energy and the specific heat per site for such systems in Fig. S10. Whereas the bulk system's internal energy tends to -28.92 per site (the energy units are $J_{AB}^{(1)}$, the slab systems are unable to reach such an energy, which corresponds to a pure AFM state, the $T = 0$ bulk ground state. What can be seen from the energy is that there is a broad feature associated with the bulk first-order transition at roughly the same critical temperature ($T_C^{slab} \sim 50 K$). There is also a very sharp downturn at extremely low temperature, where the system is still trying to establish the $T = 0$ ground state. However, as it can be seen in the specific heat plots, this low-temperature plot is permeated by a lot of energy fluctuations. Since $C_V = \sigma_E/T^2$, where σ_E is the energy fluctuations, the specific heat plots (Fig. S10) reveal that there is simply a pervasive amount of energy fluctuations at low temperature preventing the settling of a distinct magnetic order, even in the presence of optimal MC algorithms.

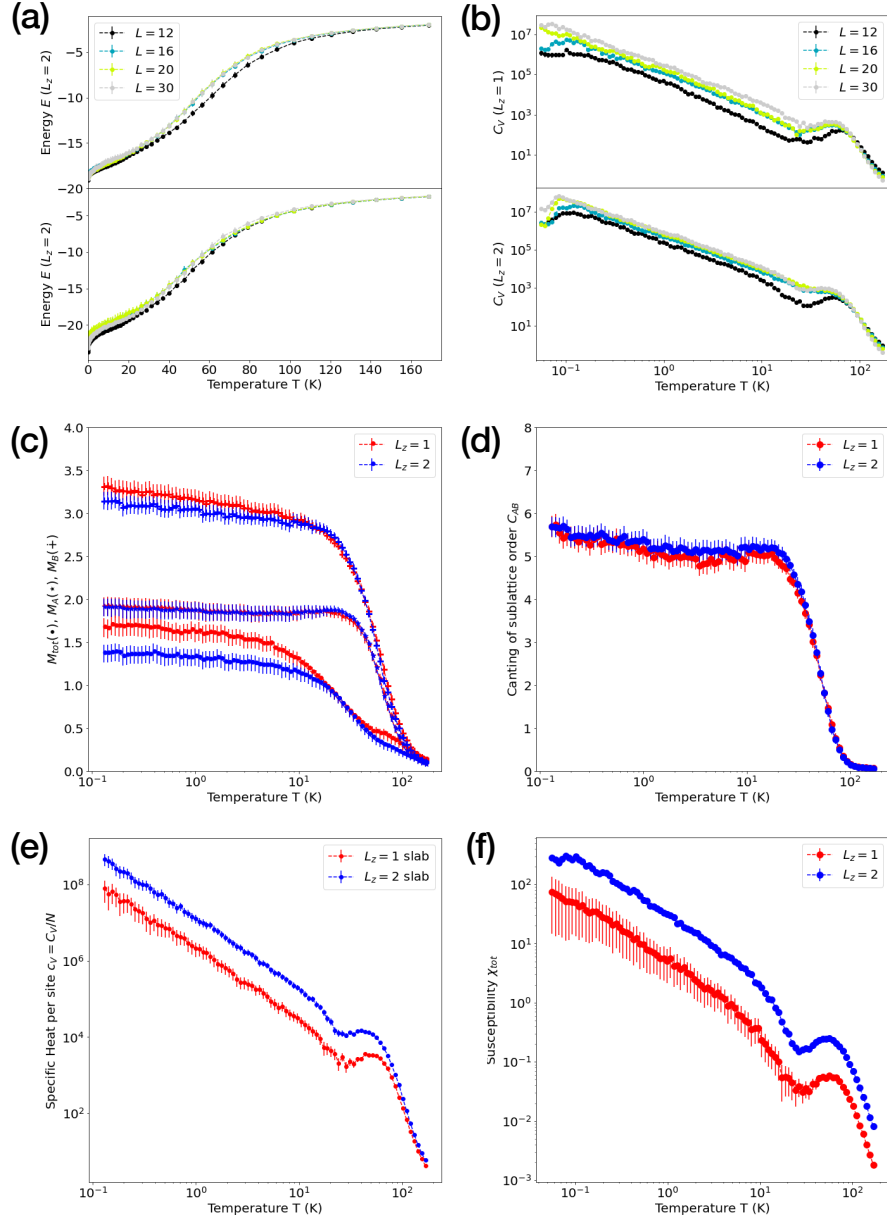


Figure S10: Thermodynamic results for the slab simulations. In the first row, results for different system sizes for $L_z = 1$ (up) and $L_z = 2$ (down), for (a) the energy per site, and (b) the specific heat. In the other figures, we show the data for $L_x = L_y = L = 30$, while varying L_z . We have (c) the magnetizations (A (start), B (plus) sublattices and total (circles)), (d) the canting angle, (e) the specific heat per site, and (f) the total susceptibility data for slab systems.

These results are also consistent with the magnetization and canting C_{AB} versus temperature data for the slab systems, which are shown in Fig. S10. In this figure, we choose to show only the results for our simulations on $L_x = L_y = 30$, our largest sample, for clarity. It is clear that although M_A is able to reach its $T = 0$ value where all A spins are aligned, the B spins cannot do the same and are plagued by large amount of fluctuations. This results in a finite canting state, but one that never really reaches the low-temperature bulk value. This is a clear indicator that the lower dimensionality samples are much more frustrated, and hence, the bulk magnetically ordered state cannot be realized.

An important question is whether we truly have achieved thermalization. In all our simulations, we performed 30,000 measurements, after each MC step, where every 100 steps we performed a parallel tempering move. In a true thermalized sample, the average value obtained in the first quarter of those measurements should not be drastically different from the one obtained in the last quarter. In Fig. S11 we show the energy per site and total magnetization for the two slab samples at $L = 30$, for 4 blocks of our measurements (each is in different colors). It is clear that none of the bins show radical departure from the others and that the averages obtained above reflect the ones of a thermalized sample. The remain large error bars are due to the computational power at our disposal.

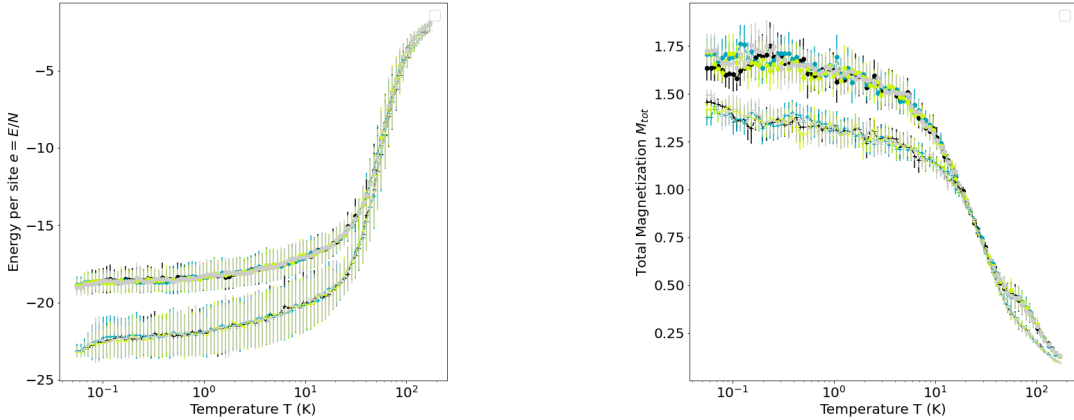


Figure S11: Measurements of the energy (left), and the total magnetization (right) for $L_z = 1$ (circles) and $L_z = 2$ (plus), for 4 different bins of the measurements.

References

- (1) X. Liu *et al.*, *Appl. Phys. Lett.* **106**, 071603 (2015).
- (2) X. Liu, S. Middey, Y. Cao, M. Kareev, and J. Chakhalian, *MRS commun.* **6**, 133-144 (2016).
- (3) R. V. Chopdekar *et al.*, *J. Magn. Magn. Mater.* **322**, 2915-2921 (2010).
- (4) G. Kresse and J. Furthmüller, *Phys. Rev. B* **54**, 11169–11186 (1996).
- (5) G. Kresse and J. Furthmüller, *Comput. Mater. Sci.* **6**, 15-50 (1996).
- (6) P. E. Blöchl, *Phys. Rev. B* **50**, 17953-17979 (1994).
- (7) G. Kresse and D. Joubert, *Phys. Rev. B* **59** 1758-1775 (1999).
- (8) J. P. Perdew, K. Burke, and M. Ernzerhof, *Phys. Rev. Lett.* **77**, 3865-3868 (1996).
- (9) S. L. Dudarev, G. A. Botton, S. Y. Savrasov, C. J. Humphreys, and A. P. Sutton, *Phys. Rev. B* **57**, 1505-1509 (1998).
- (10) I. Efthimiopoulos, Z. T. Y. Liu, S. V. Khare, P. Sarin, T. Lochbiler, V. Tsurkan, A. Loidl, D. Popov, and Y. Wang, *Phys. Rev. B* **92**, 064108 (2015).
- (11) C. Ederer and M. Komelj, *Phys. Rev. B* **76**, 064409 (2007).
- (12) L. Wang, T. Maxisch, and G. Ceder, *Phys. Rev. B* **73**, 195107 (2006).
- (13) G. Lawes, B. Melot, K. Page, C. Ederer, M. A. Hayward, Th. Proffen, and R. Seshadri, *Phys. Rev. B* **74**, 024413 (2006).
- (14) J. A. Heuver, A. Scaramucci, Y. Blickenstorfer, S. Matzen, N. A. Spaldin, C. Ederer, and B. Noheda, *Phys. Rev. B* **92**, 214429 (2015).
- (15) D. H. Lyons, T. A. Kaplan, K. Dwight, and N. Menyuk. *Phys. Rev.* **126**, 540-555 (1962).
- (16) X. Liu *et al.* *Nano Lett.* **19**, 8381-8387 (2019).

- (17) Helmut G. Katzgraber, *arXiv*: 0905.1629.
- (18) G. T. Barkema and M. E. J. Newman, *arXiv*: cond-mat/9703179.
- (19) D. J. Earl and M. W. Deem, *Phys. Chem. Chem. Phys.* **7**, 3910 (2005).
- (20) N. Rathore, M. Chopra, and J. J. de Pablo. *J. Chem. Phys.* **122**, 024111 (2005).
- (21) W Keith Hastings, *Biometrika* **57**, 97-109 (1970).
- (22) J. D. Alzate-Cardona, D. Sabogal-Suárez, R. F. L. Evans, and E. Restrepo-Parra, *J. Phys.: Condens. Matter* **31**, 095802 (2019).